A&A, 707, A253 (2026)
https://doi.org/10.1051/0004-6361/202557856

Astronomy & Astrophysics

X-Shooting ULLYSES: Massive stars at low metallicity

XIV. Properties of SMC late-O and B supergiants reveal the metallicity dependence of winds in the Magellanic Clouds

T. Alkousa[1,⋆], P. A. Crowther[1], J. M. Bestenlehner[1,2], H. Sana[3], F. Tramper[4], J. S. Vink[5], F. Najarro[4], A. A. C. Sander[6,7], M. Bernini-Peron[6], L. Oskinova[8], J. Th. van Loon[9], R. Kuiper[10], and The XShootU collaboration

[1] Astrophysics Research Cluster, School of Mathematical and Physical Sciences, University of Sheffield, Hicks Building, Hounsfield Road, Sheffield S3 7RH, UK
[2] School of Chemical, Materials and Biological Engineering, University of Sheffield, Sir Robert Hadfield Building, Mappin Street, Sheffield S1 3JD, UK
[3] Institute of Astronomy, KU Leuven, Celestijnenlaan 200D, 3001 Leuven, Belgium
[4] Departamento de Astrofísica, Centro de Astrobiología, (CSIC-INTA), Ctra. Torrejón a Ajalvir, km 4, 28850 Torrejón de Ardoz, Madrid, Spain
[5] Armagh Observatory and Planetarium, College Hill, Armagh BT61 9DG, UK
[6] Zentrum für Astronomie der Universität Heidelberg, Astronomisches Rechen-Institut, Mönchhofstr. 12–14, 69120 Heidelberg, Germany
[7] Interdisziplinäres Zentrum für Wissenschaftliches Rechnen, Universität Heidelberg, Im Neuenheimer Feld 225, 69120 Heidelberg, Germany
[8] Institut für Physik und Astronomie, Universität Potsdam, Karl-Liebknecht-Str 24/25, 14476 Potsdam, Germany
[9] Lennard-Jones Laboratories, Keele University ST5 5BG, UK
[10] Faculty of Physics, University of Duisburg-Essen, Lotharstraße 1, 47057 Duisburg, Germany

Received 27 October 2025 / Accepted 28 January 2026

ABSTRACT

Context. Hot massive stars lose mass through radiation-driven winds, producing significant chemical, radiative, and mechanical feedback in the surrounding environment. The properties of these winds play a crucial role in determining the star's evolutionary path. Considering the physics of radiation-driven winds, the wind properties should depend on the metal content of the stellar atmosphere. Therefore, studying the wind properties of massive stars in different metallicities (Z) provides a sanity check on prescriptions that are widely used in evolutionary calculations.

Aims. We first aim to obtain the stellar and wind properties of a sample of late-O and B supergiants in the Small Magellanic Cloud (SMC). Using these properties, we aim to quantify the dependence of wind properties on metallicity by comparing them with those of a Large Magellanic Cloud (LMC) counterpart study, which has a similar sample and data, and employed the same modelling techniques used in this study.

Methods. Spectroscopic modelling of UV and optical data from ULLYSES and XShootU was performed using the radiative transfer code CMFGEN. We also employed an updated Bayesian inference method similar to BONNSAI to explore the evolutionary history of our sample.

Results. We derived the stellar and wind properties of 20 late-O and B supergiants. We derived the following metallicity-dependent recipe for wind momentum: $\log D_{\rm mom} = (1.64 - 0.75 \log Z/Z_{\odot}) \log (L_{\rm bol}/10^6\,L_{\odot}) + 1.38 \log Z/Z_{\odot} + 29.17$, which is applicable for $5.4 \leq \log L_{\rm bol}/L_{\odot} \leq 6.1$ and $14 \leq T_{\rm eff}/{\rm kK} \leq 32$.

Conclusions. We find a significant dependence of the wind momentum on the metallicity, which is largely due to the mass-loss rates. We do not find any evidence of a discontinuity in either the mass-loss rate or the ratio of the terminal wind velocity to the escape velocity, $\varv_{\infty}/\varv_{\rm esc}$, between 25 and 21 kK, which could be attributed to the bi-stability jump, although when taking into account the effect of luminosity in the transformed mass-loss rate, the behaviour appears to be different. Stellar parameters are consistent across different methods and radiative transfer codes, whereas mass-loss rates differ significantly with our values being generally lower. We find a discrepancy between the evolutionary and spectroscopic masses in 40% of our sample, with the evolutionary mass usually being systematically higher. The mass-loss rates of blue supergiants are far too low to strip the stellar envelope and the subsequent formation of classical Wolf-Rayet (WR) stars, leading to the conclusion that luminous blue variable eruptions or binary interactions are necessary to explain characteristics of the WR population in the SMC.

Key words. stars: atmospheres – stars: early-type – stars: massive – stars: mass-loss – supergiants – stars: winds, outflows

---

[⋆] Corresponding author: `Talkousa1@sheffield.ac.uk`

1. Introduction

Massive stars ($M > 8\,M_{\odot}$) possess strong outflows of material, which form due to the immense radiative pressure overtaking the force of gravity at the outer layers of the star. This allows the star's atmosphere to expand beyond the boundaries of the photosphere. The properties of these outflows are strongly correlated to the ratio of luminosity to mass of the star (Eddington 1926). To overcome gravity, the acceleration due to free electrons has to be combined with so-called 'line-driving', i.e. momentum transfer from radiation absorbed (and re-emitted) in spectral lines (Lucy & Solomon 1970; Castor et al. 1975). This means that the momentum driving the winds of massive stars is transferred via spectral lines. This leads to the conclusion that the chemical content of the star, or the metallicity (Z), plays an important role in determining the properties of the winds (Abbott 1982). This is particularly true for metals, and especially iron-like species, which account for the majority of line driving. This is due to their complex atomic structure and the large number of line transitions in their ions.

The theory of line-driven wind and its implications for the Z dependence of wind properties have been studied in the literature. It is taken into account in the various numerical mass-loss recipes (e.g. Vink et al. 1999, 2001; Krtička et al. 2021). The Z dependence of mass-loss and wind velocity has also been well established observationally (e.g. Kudritzki et al. 1987; Prinja & Crowther 1998; Mokiem et al. 2007; Ramachandran et al. 2019; Hawcroft et al. 2024b). Nevertheless, there is a persistent discrepancy between the Z dependence that is predicted in theory and what is empirically derived from observations of blue supergiants in low-Z environments (Krtička et al. 2024).

The effects of Z extend beyond the academic interest in the wind properties of massive stars. Mass loss in massive stars is one of the factors that determines the evolutionary path of the star, including whether it is fated to explode in a type of core-collapse supernova (ccSNe II/Ib/Ic) and leave behind a black hole (BH) or a neutron star (NS) remnant (Smartt 2009), or whether it would experience direct collapse into a BH in a failed-nova scenario (for a review of the effects of mass-loss on the evolution of massive stars, see e.g. Smith 2014).

The winds of massive stars also play an important role in the chemical evolution of their host galaxies by enriching the interstellar medium (ISM) with heavy elements that are synthesised in their interiors and are transported to the surface of the star via efficient internal mixing processes (Langer 2012). The mass ejected via stellar winds propagates through the ISM at supersonic speeds, leading to strong mechanical feedback to the surroundings of massive stars. This, in addition to the enrichment of the ISM in heavy elements, leads to an increase in its opacity, affecting the star formation rate in the host galaxy (for a general review on massive star feedback see e.g. Geen et al. 2023).

Due to the abundant metal lines in B-type supergiants, they have been used to constrain heavy metal content in extragalactic environments (Urbaneja et al. 2005a,b; Trundle et al. 2004; Trundle & Lennon 2005; Bresolin et al. 2022). They have also been successfully used as distance indicators in external galaxies due to their high visual brightness (Kudritzki et al. 2003, 2024).

This study was made possible by the advent of the Hubble Ultra-violet Legacy Library of Young Stars as Essential Standards (HST ULLYSES, Roman-Duval et al. 2025). The HST ULLYSES programme dedicated 500 orbits to obtain high-resolution UV spectra of OB stars in low-Z environments, mainly the Large Magellanic Cloud (LMC) and Small Magellanic Cloud (SMC). The UV range is critical for determining the properties of the wind, but it lacks information about the underlying photosphere. For a fuller picture of the stellar and wind properties, we made use of the XShooting/ULLYSES optical spectroscopic legacy library (XShootU, Sana et al. 2024).

Recent efforts have been made by Marcolino et al. (2022), Backs et al. (2024), and Pauli et al. (2025) to constrain the Z dependence of wind properties and to produce empirical recipes for mass loss and wind momentum. These recipes, although very insightful, suffer from different issues. In particular, these recipes are produced using assumptions inferred from numerical recipes (Leitherer et al. 1992; Vink et al. 2001; Krtička et al. 2021; Björklund et al. 2023). Furthermore, luminosity classes are not taken into account in these recipes. Lastly, empirical recipes usually use results from the literature, which use different atmosphere codes and various datasets, some UV and optical, and some only optical, subjecting the derived parameters to large variance (Sander et al. 2024).

The present study may be viewed as the second in a series of papers, following Alkousa et al. (2025, henceforth Paper XIII), in which a sample of LMC late-O and B supergiants was analysed. In the present study, we expand our analysis of OB stars to the SMC. We aim to quantify the effect of Z on the properties of the wind. We do not aim to produce a full empirical recipe dependent on Z of mass loss, as doing this without forcing any assumptions from numerical simulations would require another Z environment, such as the Milky Way (MW), which we aim to undertake in a future study.

The XShootU and ULLYSES datasets have been used in recent studies of OB supergiants in the SMC, employing various radiative transfer codes and fitting techniques for different purposes. We compare our derived photospheric and wind parameters to those obtained by Bestenlehner et al. (2025), Backs et al. (2024), and Bernini-Peron et al. (2024) in Appendix F.

In Section 2, we present the dataset that was used in this study, our sample, and our selection criteria. In Section 3, we give a summary of our methodology, which was presented in Paper XIII in thorough detail. In Section 4, we introduce the results of our analysis. In Section 5, we discuss the implications of our results, including the effects of Z and the bi-stability jump.

2. Observations

In Table 1, we present the stars in our sample, along with their classification, which was adopted from Bestenlehner et al. (2025). In this table, we also include the telescope, instrument, and wavelength coverage available for each star.

This sample was selected in such a way that it would cover a spectral range similar to that of Paper XIII. We cover a wide range of spectral classes, from O9 to B8, which includes the region of the theorised bi-stability jump. We attempted to include more than one star per spectral class, ideally with different luminosity classifications (Ia^{+}, Ia, Iab, Ib). This allowed us to explore the Z dependence of wind properties while avoiding selection bias, which we discussed in Paper XIII when contrasting our results for the LMC sample with the results of Bernini-Peron et al. (2024) in the SMC, whose sample was made up almost exclusively of Ia supergiants. We have ten stars in common with Bernini-Peron et al. (2024), who include eight stars that are not covered in our study, while we include ten stars not covered in Bernini-Peron et al. (2024). That makes the two studies complementary, although with slightly varying modelling techniques (X-rays and micro-turbulence), and an excellent opportunity to compare the results in our overlapping samples.

Table 1. List of the stars included in our analysis and the respective wavelength coverage.

Star	Alias	SpT	(900–1160) FUSE	(1150–1700) HST	(1700–2370) HST	Aux. Opt. Magellan
AzV 469	Sk 148	O9 Iab(f)	LWRS	STIS E140M	–	–
AzV 372	Sk 116	O9.2 Iab	LWRS	STIS E140M	STIS E230M	–
AzV 456	Sk 143	O9.5 Iab	LWRS	COS G130M+G160M	STIS E230M	–
AzV 327	R 28, BLOeM 1-066	O9.7 Ib	LWRS	STIS E140M	–	MIKE
AzV 235	R 17, Sk 82, BLOeM 7-064	B0 Ia	LWRS	STIS E140M	STIS E230M	–
AzV 215	Sk 76	B0 Ia	LWRS	STIS E140M	STIS E230M	–
AzV 104	–	B0.5 Ia	LWRS	STIS E140M	STIS E230M	MIKE
AzV 410	–	B0.7 Iab	–	STIS E140M	–	–
AzV 242	R 18, Sk 85, BLOeM 4-078	B0.7 Ia	LWRS	STIS E140M	STIS E230M	-
AzV 96	Sk 46, BLOeM 8-008	B1 Iab	LWRS	STIS E140M	STIS E230M	MIKE
AzV 264	Sk 94, BLOeM 1-009	B1 Ia	LWRS	STIS E140M	STIS E230M	MIKE
AzV 175	Sk 64	B1.5 Ib	LWRS	COS G130M+G160M	-	MIKE
Sk 191	–	B1.5 Ia	LWRS	STIS E140M	STIS E230M	–
AzV 18	Sk 13	B2 Ia	LWRS	STIS E140M	STIS E230M	MIKE
NGC330 ELS 4	Rob B37	B2.5 Ib	–	STIS E140M	STIS E230M	MIKE
AzV 187	Sk 68	B2.5 Ia	LWRS	COS G130M+G160M	STIS E230M	MIKE
AzV 22	2dFS 5015	B3 Ia	–	STIS E140M	STIS E230M	–
AzV 393	R 39, Sk 124	B3 Ia^{+}	LWRS	COS G130M+G160M	STIS E230M	MIKE
AzV 343	Sk 111	B8 Iab	–	COS G130M+G160M	STIS E230M	MIKE
AzV 324	BLOeM 1-062	B8 Ib	–	COS G130M+G160M	STIS E230M	–

Notes. The spectral types are based on XShootU observations (Bestenlehner et al. 2025).

A subset of our sample has been included in the BLOeM survey (Shenar et al. 2024). Britavskiy et al. (2025) did not find evidence of significant radial velocity shifts across nine epochs of this subset, indicating that these stars are apparently single. They report that AzV 242 (BLOeM 4-078) and AzV 96 (BLOeM 8-008) show intrinsic line profile variability, with the possibility that AzV 242 is an SB1 spectroscopic binary.

2.1. ULLYSES

The ULLYSES programme (Roman-Duval et al. 2025) made use of two instruments aboard HST ; namely, the Cosmic Origins Spectrograph (COS, Green et al. 2012) in the G130M/1291, G160M/1611, and G185M/1953 wavelength settings, achieving a minimum spectral resolving power of $R \approx 12\,000$, $R \approx 13\,000$, and $R \approx 16\,000$, respectively, and the Space Telescope Imaging Spectrograph (STIS, Woodgate et al. 1998) E140M/1425 ($R \approx 46\,000$), and E230M/1978 ($R \approx 30\,000$) gratings in the far- and near-UV. New COS and STIS spectra were obtained for a subset of our targets between July 2020 and Sept 2022, and were combined with archival HST spectra drawn from GO 7437 (PI: Lennon), GO 9116 (PI: Lennon), GO 12581 (PI: Roman-Duval), GO 13778 (PI: Jenkins), and GO 15837 (PI: Oskinova) obtained between Oct 2001 and Jun 2020. A subset of HST spectra have previously been presented by Walborn et al. (2000) and Evans et al. (2004).

Archival spectra from the Far Ultra-violet Spectroscopic Explorer (FUSE, Moos et al. 2000) cover the wavelength range of ≈900–1160 Å and uniformly involve the LWRS ($30'' \times 30''$) aperture for our sample, providing $R \approx 15\,000$. These are drawn from various Principal Investigator Team and Guest Investigator programmes obtained between May 2000 and July 2003. FUSE spectroscopy of a subset of the current sample has previously been presented by Walborn et al. (2002). We note that AzV 327 lies in a crowded region, such that other sources, including [M2002] SMC 55495, contribute to the FUSE spectrum (Danforth et al. 2002).

2.2. XShootU

ULLYSES targets were observed using the X-shooter instrument (Vernet et al. 2011), which is mounted on the Very Large Telescope (VLT). This slit-fed spectrograph ($11''$ slit length) provides simultaneous coverage of the wavelength region between 3000–10 200 Å, across two arms: UVB ($3000 \leq \lambda \leq 5600$ Å) and VIS ($5600 \leq \lambda \leq 10\,200$ Å). The observations were carried out between October and December 2020 with a slit width $0.8''$ for the UBV arm, achieving $R \approx 6700$, and $0.7''$ for the VIS arm, with $R \approx 11\,400$ (Vink et al. 2023). All science-ready optical spectra used in this study were combined, flux-calibrated, corrected for telluric contamination, and normalised by Sana et al. (2024, DR1), except for archival X-shooter spectroscopy of AzV 187 from November 2013, which we normalised using a higher-order polynomial fit of points selected around regions of clean continuum.

2.3. Photometry

The photometric magnitudes used in this study were taken from the compilation in Vink et al. (2023) to derive the bolometric luminosities by fitting the SED spectral energy distribution. The UBV photometry was taken from Ardeberg & Maurice (1977), Azzopardi et al. (1975), Ardeberg (1980), and Massey (2002), and the JKs photometry was drawn from the VISTA near-infrared YJK_S survey of the Magellanic System (VMC, Cioni et al. 2011), with H-band photometry taken from the Two Micron All Sky Survey (2MASS, Cutri et al. 2003; Skrutskie et al. 2006; Cutri et al. 2012).

2.4. MIKE spectroscopy

High-resolution optical spectroscopy used to extract the rotational properties of slow rotators was collected between December 2021 and December 2022 using the Magellan Inamori Kyocera Echelle (MIKE) spectrograph mounted on the Magellan Clay 6.5 m Telescope, covering the wavelengths 3350 to 5000 Å in the blue arm and 4900 to 9500 Å in the red arm, achieving $R \approx 35\,000$–$40\,000$ (Crowther 2024).

3. Methods

In this section, we present a summary of the modelling and fitting techniques used in our analysis. In the present study, we employ the same strategies as in Paper XIII. Therefore, for a comprehensive and detailed description of our methodology, we refer the reader to Paper XIII.

3.1. Model atmosphere and grid

We employed the 1D radiative transfer code CMFGEN (Hillier 1990; Hillier & Miller 1998), which solves the radiative transfer equations in spherical symmetry in non-local thermodynamic equilibrium (non-LTE), taking into account the effects of mass loss under the assumption of purely radial outflows. CMFGEN also accounts for the effects of extreme UV blanketing caused by millions of lines of iron-like species and other elements on populations and the ionisation structure in the wind. This is implemented using super-levels (Anderson 1985, 1989), which allow for the bundling of levels with similar energies and properties into a single or a super-level. This significantly reduces the number of statistical equilibrium equations that must be explicitly solved.

CMFGEN does not calculate the velocity stratification in the wind consistently with radiative acceleration, but rather superimposes a velocity law with a simple β parametrisation. Additionally, wind inhomogeneities are considered under the 'optically thin clumping' approximation, or micro-clumping, assuming that these optically thin clumps are smaller than the mean free path of the photons (Hillier 1996) and that the medium between the clumps is completely void of matter (Hillier 1997; Hillier & Miller 1999).

In Table 2, we present the properties of our grid. The effective temperature, T_eff, surface gravities, $\log(g/\mathrm{cm\,s^{-2}})$, and mass-loss rates, $\log(\dot{M}/M_\odot\,\mathrm{yr^{-1}})$, were refined starting from the preferred grid model. Other parameters, such as elemental abundances ($\epsilon_\mathrm{X} = \log X/H + 12$), wind acceleration parameter, β, volume filling factor, $f_\mathrm{vol,\infty}$, and terminal wind velocity, v_∞, were fixed in the grid, but were later fine-tuned for each star. Stars that have T_eff or $\log g$ values outside of the range covered by the grid were handled by building miniature grids and using those grids to fine-tune the model parameters.

The atomic model and data used in this study are identical to those shown in Table C.1 in Paper XIII. We included 14 species and 50 different ions. In cooler models (<25 kK), we omitted higher ionisation stages and included the lower ionisation stages. This is important for model convergence and for the iron forest in the UV spectra of B stars.

Also, similarly to Paper XIII, we excluded X-rays from our fitting procedure to guarantee a homogeneous analysis without variations in the techniques. X-rays, which were included in Bernini-Peron et al. (2024), increase the population of high ionisation stages (super-ionisation), affecting the strength of P Cygni resonance lines in the UV, such as N v λ1238, 1242, Si IV λλ1394, 1403, and C IV λλ1548, 1551. The super-ionisation comes at the expense of depopulating the lower ionisation stages, affecting lines of Al III and C II.

Table 2. CMFGEN SMC-metallicity grid parameters.

Iterated parameters		
Parameter	Values	Step
$\log(T_\mathrm{eff}/\mathrm{K})$	$4.150 \cdots 4.600$	0.025
$\log(g/\mathrm{cm\,s^{-2}})$	$1.7 \cdots 3.9$	0.2
$\log(\dot{M}/M_\odot\,\mathrm{yr^{-1}})$	$-7.0 \cdots -5.5$	0.3
Fixed parameters		
Parameter	Value	
$\log(L/L_\odot)$	5.8	
β	1.0	
$f_\mathrm{vol,\infty}$	0.1	
ϵ_C	7.42	
ϵ_N	6.66	
ϵ_O	8.05	
ϵ_Ne	7.23	
ϵ_Mg	6.78	
ϵ_Al	5.59	
ϵ_Si	6.72	
ϵ_P	5.11	
ϵ_S	6.36	
ϵ_Ca	5.61	
ϵ_Fe	6.80	
ϵ_Ni	5.37	
Dependent parameters		
$v_\infty(T_\mathrm{eff})$	Hawcroft et al. (2024b) recipe	

Notes. The values for abundance were adopted from Vink et al. (2023), who obtained a mean baseline SMC from multiple studies that derived the elemental abundances using different methods.

In our grid, we choose a simple modified β velocity law that was introduced in Castor & Lamers (1979):

$$v(r) = v_0 + (v_\infty - v_0)\left(1 - \frac{R_*}{r}\right)^{\beta}, \tag{1}$$

where v_∞ is the terminal wind velocity, v_0 is the connection velocity, which is estimated as two-thirds the speed of sound $\approx 10\ \mathrm{km\,s^{-1}}$, and R_* is the radius of the star, which is defined at the Rosseland optical depth $\tau = 100$. The velocity adopted for each point on the grid was obtained via the T_eff and Z-dependent empirical recipe from Hawcroft et al. (2024b):

$$\begin{aligned} v_\infty\,(\mathrm{km\,s^{-1}}) = {} & [0.092(\pm0.003)T_\mathrm{eff}\,(\mathrm{K}) \\ & -1040(\pm100)]\,Z/Z_\odot^{(0.22\pm0.03)}, \end{aligned} \tag{2}$$

which was derived from Sobolev with exact integration (SEI) modelling of the P Cygni resonance doublet C IV λλ1548–1551 to measure the terminal wind velocity. We adopted $Z = 0.2\,Z_\odot$ in Equation (2) (Vink et al. 2023).

To account for wind inhomogeneity, we adopted an exponential clumping law of the form

$$f(r) = f_\mathrm{vol,\infty} + (1 - f_\mathrm{vol,\infty})\exp\left(-\frac{v(r)}{v_\mathrm{cl}}\right), \tag{3}$$

where $f_{\mathrm{vol},\infty}$ is the terminal volume-filling factor and υ_{cl} is the onset clumping velocity. We adopted the values $f_{\mathrm{vol},\infty} = 0.1$ and $\beta = 1$ in the grid, both of which were later modified in the fine-tuning process to obtain satisfactory fits for the Hα and UV P Cygni lines.

The grid spans a range for the transformed radius, $\log R_t$ (Schmutz et al. 1989), of between 2.1 and 4.0 on a logarithmic scale, where $R_t = R_*(\upsilon_\infty\, \dot{M}^{-1}\, f_{\mathrm{vol}}^{0.5}\, 10^{-4}\, M_\odot \mathrm{yr}^{-1}/2500\,\mathrm{km\,s^{-1}})^{2/3}$, with smaller values relating to denser winds. This $\log R_t$ range corresponds to a range of optical depth-invariant wind-strength parameters, $\log Q = \log \dot{M}/(R_* \upsilon_\infty)^{3/2}$ (Puls et al. 1996), of -15.0 to -12.5, where larger values of $\log Q$ correspond to denser winds. We employed R_t to scale $\dot{M}$ to the derived bolometric luminosity of the star.

3.2. Fitting procedure and diagnostics

We first used the results of Bestenlehner et al. (2025) to pinpoint the closest fitting model on the grid in $\log T_{\mathrm{eff}}$-$\log g$-$\log \dot{M}$ parameter space, after which we start the fine-tuning procedure. The analysis in Bestenlehner et al. (2025) is based on the model de-idealisation pipeline, which applies a minimisation and interpolation routine using a large grid of FASTWIND models (Puls et al. 2005; Rivero González et al. 2011). This allows for the estimation of stellar parameters and the mass-loss rates and model uncertainties using only optical spectroscopy (Bestenlehner et al. 2024).

Once we selected the nearest grid model, we started by fine-tuning the values of T_{eff}, $\log g$, and the helium abundance iteratively until a satisfactory fit was achieved. Then we iteratively fine-tuned $\log \dot{M}$, β, $f_{\mathrm{vol},\infty}$, and υ_∞ to fit Hα and the UV P Cygni lines. Finally, the CNO mass fractions were fine-tuned for each star.

Here, we give a summary of the fitting procedure. The approach for determining the goodness of the fit was 'χ-by-eye'. For an extensive description of the fitting techniques, diagnostics, and uncertainty determination, we refer the reader to Section 3 of Paper XIII.

Effective temperature, T_{eff}. We obtained the effective temperature from the principle of ionisation equilibrium. In O supergiants the primary T_{eff} diagnostics are He I λ4471–He II λ4542 (Martins 2011). For early and mid-B supergiants, we used ratios of adjacent ions of silicon as primary diagnostics (McErlean et al. 1999); namely, Si IV $\lambda\lambda$4088–4116 versus Si III $\lambda\lambda\lambda$4553–4568–4575 for B0 to B2 stars, and Si III $\lambda\lambda\lambda$4553–4568–4575 versus Si II $\lambda\lambda$4128–4131 for B2.5–B3 stars. Note that in early B stars the Si IV λ4088.96 line is blended with O II λ4089.29 (Hardorp & Scholz 1970; de Burgos et al. 2024b), so we ensured that this transition is accounted for in the adopted atomic model. For B8 supergiants, we used the ratio of He Iλ4471 to Mg II λ4481 to determine T_{eff}.

Surface gravity $\log g$. We determined the surface gravity by fitting the wings of Balmer lines, which are very sensitive to Stark broadening. The primary $\log g$ diagnostics for all stars in our sample are Hγ, Hη, and Hζ. These lines are relatively isolated – in contrast with Hδ – and are usually not contaminated by wind effects (Lennon et al. 1992).

Luminosity. To determine the bolometric luminosity, L_{bol}, of stars, we used the model fluxes (which were calculated for $\log L_{\mathrm{model}}/L_\odot = 5.8$). The reddening law from Gordon et al. (2003) was then applied to the model fluxes. We then fitted the relative extinction, R_V, and other parameters that determine the shape of the UV extinction curve (Fitzpatrick & Massa 1990). Then the intrinsic colours were obtained (B^m, V^m, and Ks^m) by applying filter functions from PYPHOT (Fouesneau 2025) to the model SED using the Vega magnitude system photometric zero-point (for more details on PYPHOT, see Table 3 in Paper XIII). The colour excess $E(B-V)$ was calculated as $(B-V)-(B^m-V^m)$. The model SED was then scaled to match observations using a factor equal to the ratio of Ks fluxes F^m_{Ks}/F_{Ks}. The bolometric correction, BC_V, was calculated as $-2.5\log L_{\mathrm{model}} + 4.74 - V^m$. The final L_{bol} was calculated as $(DM + A_V - BC^m_V - m_V + 4.74)/2.5$, where $A_V = R_V \cdot E(B-V)$, and assuming a distance modulus of $DM = 18.96$ (corresponding to a distance $d = 62$ kpc) for the SMC (Scowcroft et al. 2016). In other relevant XShootU studies, a value of 18.98 for the distance modulus was adopted from Graczyk et al. (2020).

Helium mass fraction. We obtained the helium abundance by fitting He I and He II lines relative to hydrogen lines. The diagnostic lines used across the sample are He I λ4026, He I λ4471, and He I λ4922 for O and B supergiants, and He II λ4542 and He II λ5411 for O supergiants. We also used He I λ6678, He I λ7065, and He I λ7281 as a sanity check.

Wind density parameters. The wind density, ρ, is defined by υ_∞, $\log \dot{M}$, $f_{\mathrm{vol},\infty}$, β, and υ_{cl}. The primary optical diagnostic line for $\log \dot{M}$ and β is Hα ($\propto \rho^2$). The UV unsaturated P Cygni profiles provide valuable information on wind inhomogeneities (Massa et al. 2008; Searle et al. 2008; Puls et al. 2008). The UV lines that we used to constrain $\log \dot{M}$ and $f_{\mathrm{vol},\infty}$ are S IV$\lambda\lambda$1063–73, C IIIλ1176, Si IV$\lambda\lambda$1394–1403, C IV $\lambda\lambda$1548–51, and Al III$\lambda\lambda$1856–62. υ_{cl} was adopted as two times the speed of sound of the model. υ_∞ was obtained from either (i) direct measurements of the black velocity, $\upsilon_{\mathrm{black}}$ (the velocity measured at the bluest extent of fully saturated P Cygni absorption (Prinja et al. 1990)), or (ii) as a fraction of υ_{edge} (the velocity measured at the point where the blue trough of the P Cygni profile intersects the local continuum (Beckman & Crivellari 1985)). We present the results of the velocity measurement in Table. E.1.

Line broadening parameters. Absorption lines are broadened by the effect of rotation (Slettebak 1956), photospheric macroturbulence, υ_{mac} (Conti & Ebbets 1977; Simón-Díaz et al. 2010; Simón-Díaz & Herrero 2014), and micro-turbulence, υ_{mic} (McErlean et al. 1998). We fixed $\upsilon_{\mathrm{mac}} = 20\,\mathrm{km\,s^{-1}}$ and $\upsilon_{\mathrm{mic}} = 10\,\mathrm{km\,s^{-1}}$, and only determined the projected rotational velocity, $\upsilon_{\mathrm{rot}} \sin i$, using metal lines. For O stars, our primary diagnostic is O III λ5592. For early B stars, we used C III λ4267 and Si III λ4553. For mid- to late-B stars, we fitted the N II λ3995 line and, as a sanity check, we used Si II λ6347, the Mg II λ4481 doublet, and C II λ4267.

CNO abundances, ϵ_{X}. The abundances of carbon, nitrogen, and oxygen were constrained by fitting multiple optical absorption lines of each element. The selection of lines depends on the ion that dominates the photosphere in each spectral type. In Table D.1, we present our choice of diagnostic lines. The CNO abundances (among other metals) are arguably the most sensitive parameters to changes in photospheric micro-turbulent velocity, υ_{mic} (Urbaneja et al. 2005b). Fixing υ_{mic} in our analysis reduces the precision of our derived CNO abundances. This is due to the effect that changing the photospheric υ_{mic} has on the opacity, and therefore on the line strength of different components of multiplets (McErlean et al. 1998).

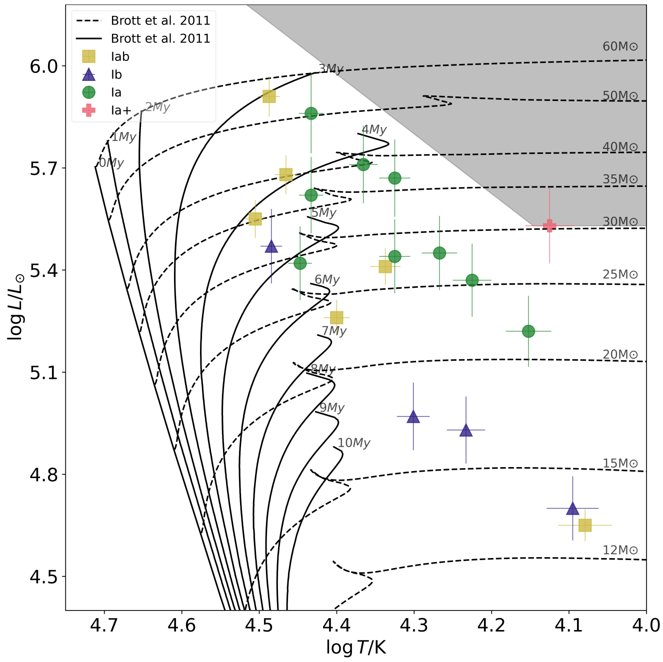

Fig. 1. Hertzsprung–Russell diagram for our sample. Overlaid in solid black lines are non-rotating SMC isochrones for different ages (≈0–10 Myr). Dashed black lines are the SMC rotating evolutionary tracks for stellar masses in the range of ≈10–60 $M_\odot$ with a rotational velocity of 110 km s^{-1}. Both the isochrones and evolutionary tracks are adopted from Brott et al. (2011). The shaded area is defined by the HD limit (Humphreys & Davidson 1979; Smith et al. 2004; Davies et al. 2018).

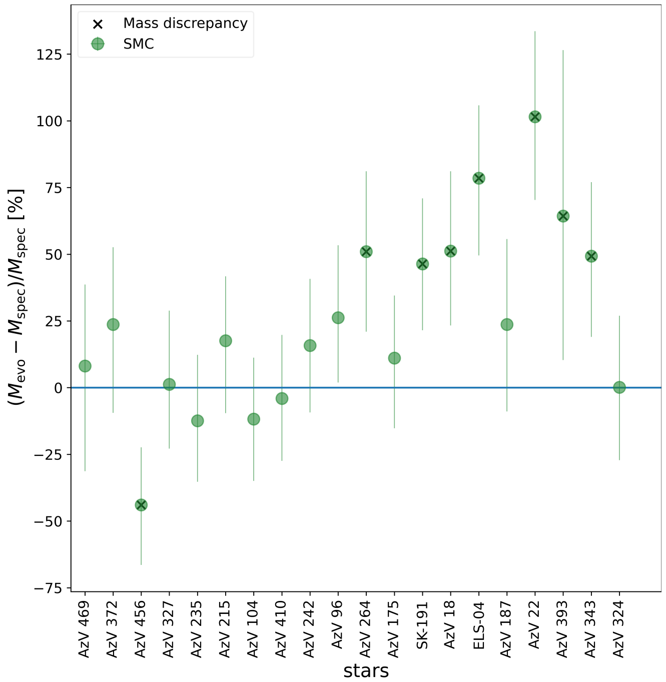

Fig. 2. Relative (percentage) difference of the evolutionary and spectroscopic masses $(M_{\rm evo} - M_{\rm spec})/M_{\rm spec}$. $M_{\rm evo}$ was obtained using a Bayesian inference method applied to SMC evolutionary models of Brott et al. (2011). The diagonal black crosses indicate the presence of a mass discrepancy.

4. Results

In this section, we present an overview of the results of our analysis. We compare our results with those from previous studies of SMC blue supergiants. In addition, we compare the derived wind parameters with predictions from numerical recipes. In Table A.1, we present the derived physical parameters and the inferred evolutionary masses and ages. In Appendix F, we compare our derived stellar and wind parameters to values from the literature. Comments on the spectral fitting quality are provided for each star individually in Appendix G. The SED fits, individual line fits, and overall spectral fits can be found in Appendix H, I, and J, respectively.

4.1. Hertzsprung-Russell diagram

Fig. 1 shows the Hertzsprung-Russell diagram (HRD) for our sample, superimposed on SMC isochrones (solid black lines) and evolutionary models (dashed black lines) (Brott et al. 2011). Our sample spans a wide range of $\log(L_{\rm bol}/L_\odot)$, from 4.65 (AzV 343) to 5.91 (AzV 456), and a $T_{\rm eff}$ range of 12.0 kK (AzV 343) to 32.0 kK (AzV 469). The shaded area in Fig. 1 is defined by the upper limit on the observed luminosities of SMC cool supergiants, also known as the Humphreys-Davidson (HD) limit (Humphreys & Davidson 1979; Smith et al. 2004; Davies et al. 2018).

As a sanity check of $T_{\rm eff}$, we compared the predicted Balmer jump strengths to observations (Kudritzki et al. 2008; Urbaneja et al. 2017). We find that the strength of the predicted Balmer jumps – the $T_{\rm eff}$ of which was obtained from the ionisation balance – agrees well with observations within a few hundred Kelvin.

The O supergiants in our sample occupy the region $\log T_{\rm eff}/{\rm kK} > 4.48$ (or $T_{\rm eff} > 30$ kK), and according to the isochrones of Brott et al. (2011) are still in their main-sequence (MS) phase. In contrast, the distribution of the cooler B supergiants ($\log T_{\rm eff}/{\rm kK} < 4.3$) on the HRD hints at them being post-MS objects, according to Brott et al. (2011) single-star evolutionary models. The evolutionary status of hot BSGs ($4.3 < \log T_{\rm eff}/{\rm kK} < 4.48$) remains ambiguous, as they are in close proximity to the terminal-age main sequence (TAMS).

4.2. Stellar masses

Spectroscopic masses, $M_{\rm spec}$, presented in Table. A.1, were calculated via $g = G\,M/R_*^2$. Since our stars are generally slow rotators, the centrifugal-force corrected gravity, $\log(g_c/{\rm cm\,s^{-2}}) = \log(g + \varv_{\rm rot} \sin i^2/R_*)$ (Herrero et al. 1992), is very similar to $\log g$. By way of example, $\log g_c - \log g = 0.02$ dex for AzV 372, which has the largest $\varv_{\rm rot} \sin i$ of our sample (100 km s^{-1}). We also present evolutionary masses, $M_{\rm evo}$, and ages, which were obtained using a Bayesian inference method (V. Bronner et al., in prep.) that is similar to BONNSAI (Schneider et al. 2014), applied to Brott et al. (2011) rotating single-star evolutionary models for SMC metallicity.

In Fig. 2, we present the relative difference between $M_{\rm spec}$ and $M_{\rm evo}$ for our sample. The error bars representing the uncertainties in Fig. 2 take into account in quadrature the uncertainty of $M_{\rm evo}$, which was obtained from the Bayesian inference method, and the uncertainty of $M_{\rm spec}$, which in relative terms sits between 25% and 35%. Generally, $M_{\rm evo}$ is larger than $M_{\rm spec}$ in our sample. We find that 40% of our sample shows a significant discrepancy between $M_{\rm spec}$ and $M_{\rm evo}$. For these stars, $M_{\rm evo}$ is larger than $M_{\rm spec}$, except for AzV 456, for which we

Table 3. Derived wind parameters.

Star	$\log L_{\rm bol}$ $L_\odot$	$\log \dot{M}$ $M_\odot\,{\rm yr}^{-1}$	v_∞ km s^{-1}	$v_{\rm esc,1-\Gamma}$ km s^{-1}	β	$f_{\rm vol,\infty}$	$v_{\rm cl}$ km s^{-1}
AzV 469	5.55	−7.00	1800	628	1.0	0.2	30
AzV 372	5.68	−6.76	1620	509	1.0	0.1	30
AzV 456	5.91	−7.57	1313	740	1.0	0.1	30
AzV 327	5.47	−8.12	1551	658	1.0	0.03	35
AzV 235	5.86	−6.66	1300	553	1.5	0.05	30
AzV 215	5.62	−7.17	1585	497	1.7	0.1	35
AzV 104	5.42	−7.75	996	637	1.0	0.1	35
AzV 410	5.26	$-7.65^\dagger$	403	564	1.0	0.1	30
AzV 242	5.71	−7.47	942	424	3.1	0.03	30
AzV 96	5.41	−7.43	758	409	2.6	0.1	30
AzV 264	5.44	−7.32	656	363	3.0	0.1	30
AzV 175	4.97	$-7.55^\dagger$	437	498	1.0	0.2	30
Sk 191	5.67	$-6.81^\dagger$	381	753	2.5	0.2	30
AzV 18	5.45	−7.19	388	310	3.5	0.1	25
NGC330-ELS-04	4.93	$-7.71^\dagger$	301	490	1.0	0.2	25
AzV 187	5.37	$-7.77^\dagger$	307	627	1.0	0.2	25
AzV 22	5.22	−6.75	160	220	2.5	0.1	25
AzV 393	5.53	−5.94	237	206	2.5	0.1	25
AzV 343	4.65	$-8.20^\dagger$	200	244	1.0	0.1	25
AzV 324	4.70	$-8.05^\dagger$	178	310	1.0	0.1	25

Notes. The † in the superscript indicates an upper limit. $\log \dot{M}$ is subject to an average uncertainty of 0.4 dex. $v_{\rm esc}$ is the escape velocity at the photosphere.

find that $M_{\rm spec}$ ($\approx 83 \pm 12\ M_\odot$) is significantly larger than $M_{\rm evo}$ ($\approx 47^{+6}_{-4}\ M_\odot$).

4.3. Wind properties

In Table 4.3, we present the derived wind parameters for our sample. The diverse nature of our sample is shown in the variety of $\log \dot{M}/M_\odot\,{\rm yr}^{-1}$, covering a range of ≈−8.20 to −5.94 dex. The highest mass-loss rate is attributed to the mid-B hypergiant AzV 393, and the lowest to the late-B supergiant AzV 343.

In Fig. 3, we present our best fits to (red solid line) Hα profiles from XShootU spectra (Sana et al. 2024, DR1). We also include Hα profiles from MIKE observations (Crowther 2024) to illustrate the typical variability of this wind line. We quantify the $\log \dot{M}$ variability via test fits to MIKE Hα observations, and obtain $\Delta \log \dot{M}/M_\odot\,{\rm yr}^{-1} = \pm 0.15$, which was taken into account when calculating the uncertainties of $\log \dot{M}$.

We obtain satisfactory fits for cases in which the Hα is fully or partially in emission, except for Sk 191, the Hα of which shows a redward radial velocity shift that is not present in other photospheric lines. In the cases in which Hα is fully in absorption, we focus on fitting the wings. In any case, when determining $\dot{M}$, we take into account the level of saturation of P Cygni profiles. Nevertheless, for cases in which Hα is fully in absorption, we consider the $\log \dot{M}$ presented in Table 4.3 as an upper limit on mass loss.

In Fig. 4, we present a comparison between our derived $\log \dot{M}$ and the mass-loss rates predicted by the numerical recipe of Vink & Sander (2021), Björklund et al. (2023), and Krtička et al. (2024), assuming $Z = 0.2\,Z_\odot$. We find that for $T_{\rm eff} \gtrsim 22$ kK all recipes perform well and match our derived $\log \dot{M}$ within the uncertainties. For $T_{\rm eff} \lesssim 22$ kK, which is believed to be the region where the predicted bi-stability jump occurs (Vink et al. 2001), the $\log \dot{M}$ from the recipe of Vink & Sander (2021) predictably become much higher than ours by ≈ 1.5 dex. The recipe of Krtička et al. (2024) continues to perform well on the cool side of the bi-stability jump, whereas the values from the recipe of Björklund et al. (2023) gradually become much smaller than our measurements.

In general, $\dot{M}$ predictions from numerical recipes agree reasonably well with each other and with empirically derived $\dot{M}$ in the O star regime, but deviate greatly from one another and from empirical $\dot{M}$ in the B star regime. Recalling the discussion of the evolutionary status of our sample in Section 4.1, we conclude that predictions from numerical recipes are valid for stars on the MS, where massive stars spend most of their lives and where most mass loss takes place. However for post-MS stars, the empirical mass loss rates behave differently than what is predicted by these numerical recipes.

Our sample spans a wide range of $v_\infty \approx 160$–1800 km s^{-1}. In Fig. 5 we show v_∞ versus $T_{\rm eff}$, with our results compared to the empirical recipe of Hawcroft et al. (2024b), results from Bernini-Peron et al. (2024), and velocities calculated from the numerical recipes of Vink & Sander (2021) and (Krtička et al. 2021). We find a difference in the slopes with similar offsets. The main caveat of this comparison is that Hawcroft et al. (2024b) obtained their results by employing the SEI method, fitting only the C IV λ1548 P Cygni for stars no later than B1 and with various luminosity classes. v_∞ prediction for $T_{\rm eff}$ values below 21 kK, therefore, should not be considered as reliable.

Table 4. Fitting parameter a (slope) and b (intercept) for Equation (4).

Study	a kK	b km s^{-1}
This study	0.08 ± 0.01	963 ± 200
(Hawcroft et al. 2024b, Entire sample)	0.09 ± 0.01	1560 ± 420
(Hawcroft et al. 2024b, OB SGs only)	0.07 ± 0.01	811 ± 300
(Bernini-Peron et al. 2024)	0.08 ± 0.02	936 ± 350

We fitted our results with a simple linear fit of the form

$$v_\infty[{\rm km\,s^{-1}}] = a T_{\rm eff}[{\rm kK}] \; - \; b[{\rm km\,s^{-1}}]. \tag{4}$$

In Table 4, we present the slope, a, and intercept, b, from Equation (4), and compare them to the results of Hawcroft et al. (2024b) and Bernini-Peron et al. (2024). We find that our derived fitting parameters are in excellent agreement with the parameters from (Hawcroft et al. 2024b) when considering only O and B supergiants. We also find excellent agreement with the results of Bernini-Peron et al. (2024).

Our velocities agree with predictions from the recipe of Vink & Sander (2021) below 25 kK, but are lower by ≈30% for temperatures above that threshold. We also find that the recipe from Krtička et al. (2021) systematically overpredicts the velocities by an average of ≈500 km s^{-1}.

Our results in Table 4.3 show that a high β (≈2.5 ± 0.6) is preferred to obtain a satisfactory fit for Hα in the cases in which it is fully or partially in emission. This agrees with the findings of Bernini-Peron et al. (2024), who require $\beta > 2$ for most of their SMC sample. Similarly, Crowther et al. (2006) obtained an average $\beta = 2$ from a sample of early Galactic B supergiants.

Due to the weakness of the winds of SMC supergiants, and consequently the lack of broad saturated P Cygni profiles in the UV and Hα emission, we were able to constrain $f_{\rm vol,\infty}$ for only

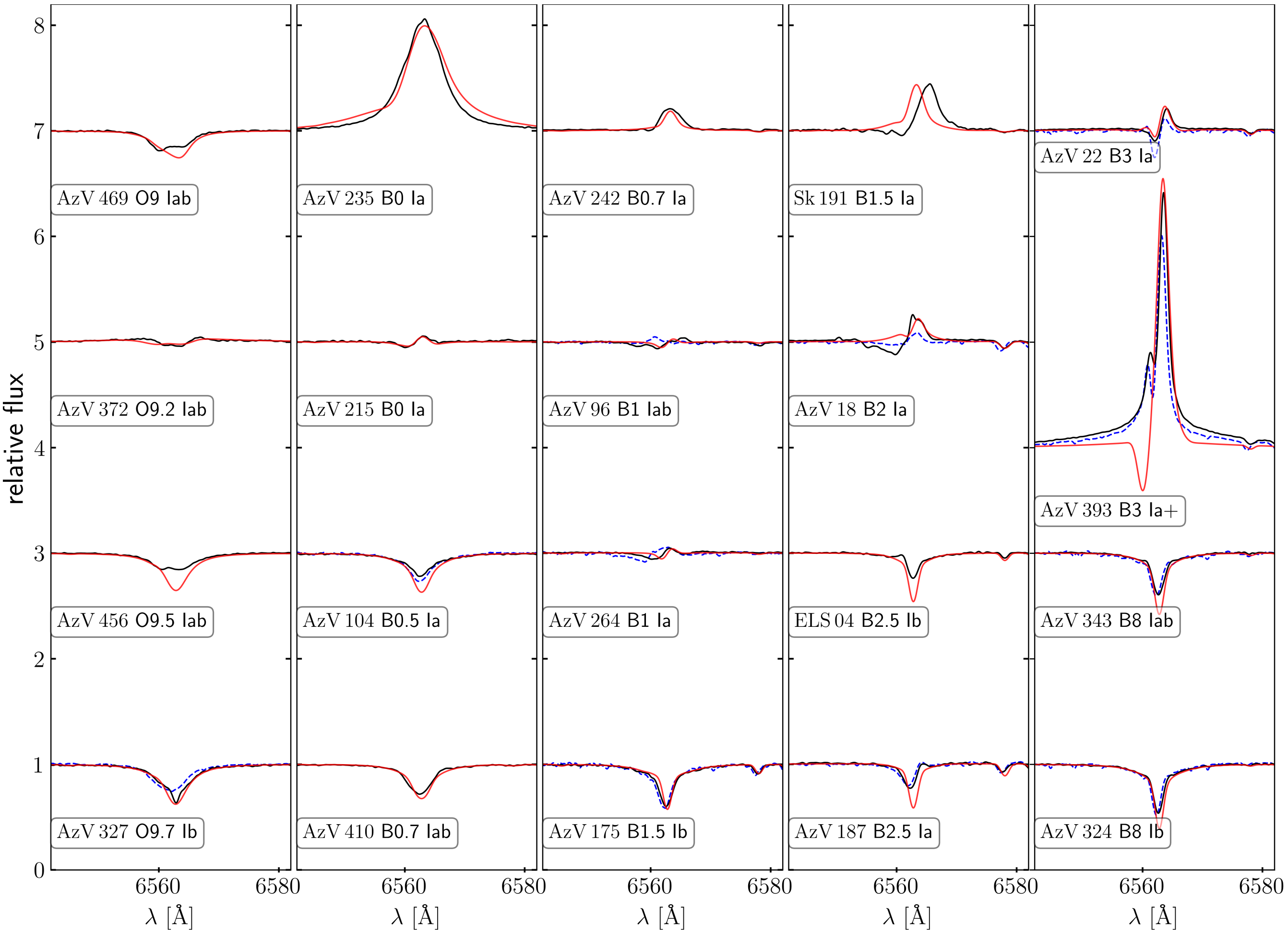

Fig. 3. Best fits (solid red lines) to XShootU Hα (+ C II λ6578) profiles (solid black lines). Magellan/MIKE spectra are also shown (dashed blue lines), where available, to illustrate line variability.

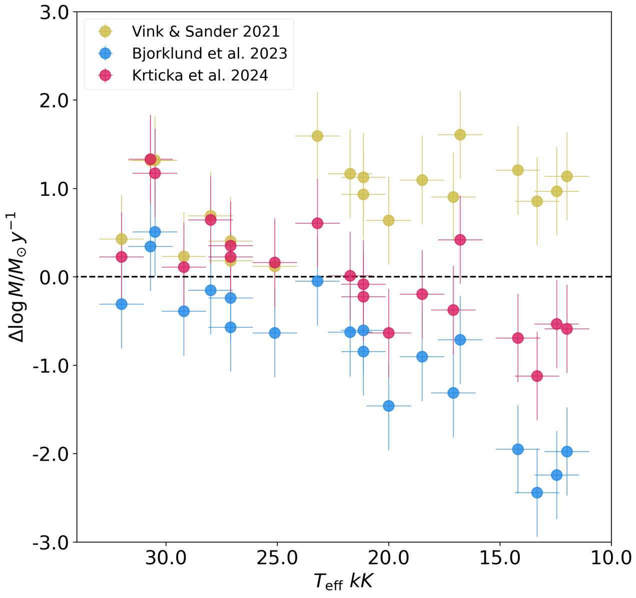

Fig. 4. $\Delta \log \dot{M}$ vs $T_{\rm eff}$. $\Delta \log \dot{M}$ is the difference between our derived $\Delta \log \dot{M}$ and those obtained from numerical recipes from Vink & Sander (2021) (yellow dots), Björklund et al. (2023) (blue dots), and Krtička et al. (2024) (red dots).

nine stars in our sample. We did not find any correlation between $f_{\rm vol,\infty}$ and $T_{\rm eff}$, $L_{\rm bol}$, or $\dot{M}$. This is similar to our findings in Paper XIII, and has been the case in recent studies conducting UV and optical spectroscopic analysis of OB stars in multiple environments and utilising various codes with different clumping implementations (Hawcroft et al. 2024a; Bernini-Peron et al. 2024; Verhamme et al. 2024; Brands et al. 2025).

4.4. Rotation

In Table A.1, we present $\upsilon_{\rm rot} \sin i$ of our sample. Our sample spans a range of $\upsilon_{\rm rot} \sin i$ from 25 km s^{-1} to 100 km s^{-1}, with a mean $\upsilon_{\rm rot} \sin i$ of 51 km s^{-1} and a standard deviation of 19 km s^{-1}. This agrees with the findings of Dufton et al. (2006), who analysed a sample of 24 SMC and Galactic B supergiants and found a linear correlation between $\upsilon_{\rm rot}$ and $T_{\rm eff}$ with a value of $\upsilon_{\rm rot} \sin i$ of ≈60 and 30 km s^{-1} for $T_{\rm eff}$ = 28 and 12 kK, respectively.

In Table 5, we compare our derived $\upsilon_{\rm rot} \sin i$ to the $\upsilon_{\rm rot} \sin i$ and $\upsilon_{\rm mac}$ that were obtained from the IACOB-BROAD tool, which employs a combined Fourier transform and goodness-of-fit approach that allows for the extraction of line-broadening parameters (Simón-Díaz & Herrero 2014). We applied IACOB-BROAD to a subsample of our stars with high-resolution MIKE data. The line we used to extract the rotational properties is

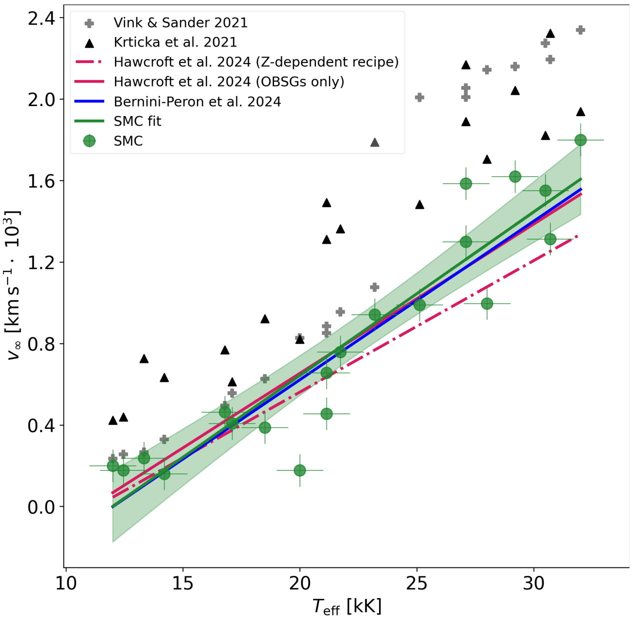

Fig. 5. v_∞ vs $T_{\rm eff}$. The green dots represent our results. The green line is the linear fit. The dashed magenta line is the Z-dependent v_∞–$T_{\rm eff}$ relation from Hawcroft et al. (2024b). The solid magenta line was obtained from fitting Hawcroft et al. (2024b) results for O and B supergiants only. The solid blue line was obtained from fitting the results of Bernini-Peron et al. (2024). The grey crosses are v_∞ calculated from Vink & Sander (2021) recipe. The black triangles represent v_∞, calculated from the recipe in Krtička et al. (2021).

Table 5. Comparison of our adopted broadening parameters with those obtained via IACOB-BROAD (Simón-Díaz & Herrero 2014) applied to high-resolution MIKE data.

Star	By eye+XShootU		IACOB-BROAD+MIKE		
	$v_{\rm rot}\sin i$ km s^{-1}	$v_{\rm mac}$ km s^{-1}	$v_{\rm rot}\sin i$ km s^{-1}	$v_{\rm mac}$ km s^{-1}	line
AzV 327	55	20	64^{+35}_{-62}	87^{+42}_{-55}	Si III λ4552
AzV 104	65	20	80^{+19}_{-53}	45^{+63}_{-43}	Si III λ4552
AzV 96	50	20	52^{+16}_{-24}	59^{+23}_{-29}	Si III λ4552
AzV 264	45	20	45^{+15}_{-43}	33^{+39}_{-31}	Si III λ4552
AzV 18	50	20	43^{+11}_{-18}	44^{+20}_{-21}	Si III λ4552
NGC330-ELS-4	35	20	33^{+9}_{-18}	29^{+19}_{-19}	Si III λ4552
AzV 187	40	20	36^{+17}_{-34}	41^{+27}_{-35}	Si III λ4552
AzV 393	30	20	35^{+16}_{-32}	30^{+33}_{-28}	Si III λ4552
AzV 343	35	20	44^{+9}_{-21}	19^{+33}_{-17}	Si II λ6347
AzV 324	25	20	21^{+6}_{-9}	26^{+8}_{-10}	Si II λ6347

Si III λ4552 for the entire subsample, except for the late B supergiants AzV 324 and AzV 343, for which we used Si II λ6347.

We find that our derived $v_{\rm rot}\sin i$ agree with those obtained from IACOB-BROAD within 10 km s^{-1}, except for AzV 104 and AzV 327, where the IACOB-BROAD $v_{\rm rot}\sin i$ is 15 and 20 km s^{-1} higher than ours, respectively. On the other hand, we tend to underestimate $v_{\rm mac}$ on average by ≈20 km s^{-1}. The largest difference in $v_{\rm mac}$ are observed in AzV 327 and AzV 96, for which the values obtained from IACOB-BROAD are higher by 67 and 39 km s^{-1}, respectively.

Table 6. Best-fitting helium (Y, by mass) and CNO ($\epsilon_{\rm X}$, by number) abundances.

Star	Y	$\epsilon_{\rm C}$	$\epsilon_{\rm N}$	$\epsilon_{\rm O}$	$\frac{\Sigma{\rm CNO}}{\Sigma{\rm CNO}_{\rm SMC}}$	$\frac{\Sigma{\rm CNO}}{\Sigma{\rm CNO}_\odot}$
AzV 469	0.52	7.3	8.1	8.2	2.2	0.42
AzV 372	0.52	7.2	7.8	8.2	1.7	0.33
AzV 456	0.30	7.2	7.2	8.1	1.0	0.19
AzV 327	0.46	7.2	7.8	8.1	1.3	0.24
AzV 235	0.30	7.0	7.8	7.9	1.0	0.19
AzV 215	0.30	7.0	8.0	8.1	1.6	0.31
AzV 104	0.30	7.0	7.7	8.0	1.0	0.20
AzV 410	0.37	7.1	7.7	8.0	1.1	0.22
AzV 242	0.30	7.0	7.5	8.0	1.0	0.18
AzV 96	0.30	6.7	7.9	7.8	0.9	0.18
AzV 264	0.46	6.8	7.9	7.8	1.1	0.21
AzV 175	0.30	7.1	7.5	8.1	1.1	0.21
Sk 191	0.43	6.9	7.9	8.0	1.2	0.23
AzV 18	0.43	7.1	7.7	8.0	1.1	0.22
NGC330-ELS-04	0.40	7.0	7.9	7.9	1.2	0.23
AzV 187	0.30	7.2	7.5	8.0	0.9	0.18
AzV 22	0.46	6.9	8.0	8.0	1.4	0.27
AzV 393	0.30	6.9	7.8	8.0	1.1	0.21
AzV 343	0.40	7.6	7.9	7.5*	1.1	0.20
AzV 324	0.34	7.2	7.6	7.5*	0.6	0.11
Averages	0.37	7.0	7.8	7.9	1.1	0.23

Notes. The uncertainties of the helium mass fraction are 10% . The adopted uncertainty of CNO abundances is ±0.3 dex. The last two columns represent the cumulative CNO mass fraction relative to the cumulative CNO SMC baseline and solar baseline, respectively. Oxygen abundance values with the asterisk subscript were obtained from fitting the O I λλλ7772–7774–7775 multiple, and are considered lower limits.

4.5. Chemical composition

We present the best-fitting chemical abundances for our sample in Table 6. We find moderate helium enhancement for our sample relative to the SMC baseline (Y~0.25, Russell & Dopita 1990), which is to be expected in a sample comprised of blue supergiants. Fig. 6 shows that all stars in our sample exhibit significant nitrogen enrichment. According to the rotating single-star evolutionary models of Brott et al. (2011) that include rotational mixing, this enrichment can be explained by the high initial rotational velocities ($v_{\rm rot}\sin i$ > 300 km s^{-1}), which cause nitrogen synthesised in the interior of the star to be transported to the surface. However, Dufton et al. (2006) found that $v_{\rm rot}\sin i$ of SMC B supergiants falls in the range of ≈60–30 km s^{-1}, whereas Mokiem et al. (2006) found that $v_{\rm rot}\sin i$ falls in the range of ≈150–180 km s^{-1} from a diverse sample of SMC O and early B stars.

Spectroscopic studies of the rotational properties of O stars in the SMC, LMC, and the MW show that most early O stars, which are the progenitors of B supergiants, are not fast rotators. Ramachandran et al. (2019) find that ≈75% of SMC O stars have $v_{\rm rot}\sin i$ < 200 km s^{-1}. In the Tarantula nebula, Ramírez-Agudelo et al. (2013) find that the distribution of $v_{\rm rot}\sin i$ of O stars peaks at ≈80 km s^{-1}. Similarly, (Holgado et al. 2022) find that the distribution of $v_{\rm rot}\sin i$ of O stars across all luminosity classes in the MW peaks at ≈80 km s^{-1}.

These observed distributions challenge the assumption that extremely high initial or current rotational velocities are the explanation for the nitrogen enhancement. Only about ≈25% of

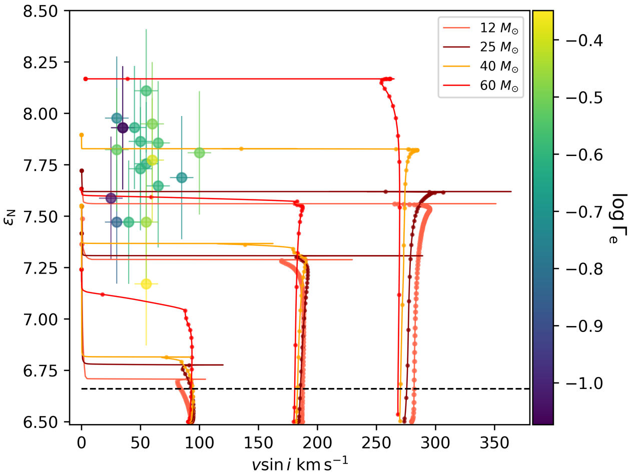

Fig. 6. ϵ_N vs $v_{\rm rot}\sin i$. The colour scheme corresponds to the value of Γ_e. The solid pink, brown, orange, and red lines represent SMC evolutionary tracks for initial masses of 12 $M_\odot$, 25 $M_\odot$, 40 $M_\odot$, and 60 $M_\odot$, respectively, with initial rotational velocities of 110, 250, 350 km s^{-1} (Brott et al. 2011). We multiplied by a factor of $\pi/4$ to take into account the inclination of the rotation axis (Hunter et al. 2008). The dashed black line represents the baseline ϵ_N in the SMC (Vink et al. 2023). The dots along the evolutionary tracks represent time steps of 0.1 Myr.

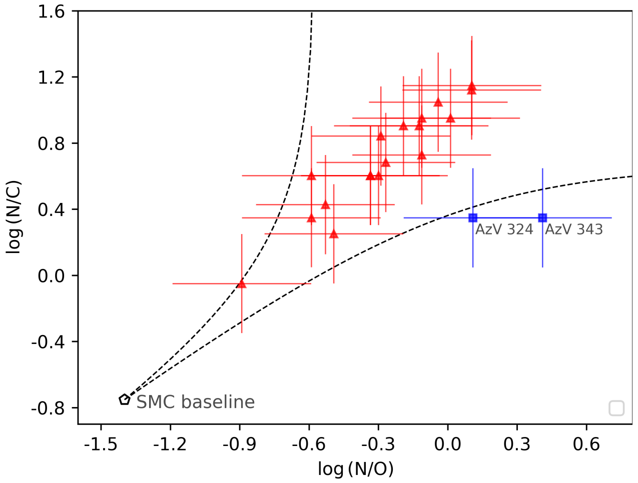

Fig. 7. log N/C vs log N/O. The red triangles show the distribution of our sample. The stars for which the oxygen abundance was obtained from fitting the O I $\lambda\lambda\lambda$7772–7774–7775 multiplet are shown in blue squares. The dashed black lines represent the upper and lower boundaries adopted from Maeder et al. (2014).

the massive stars are effectively single, with the overwhelming majority of the fastest rotators being the product of binary interaction (de Mink et al. 2013; Britavskiy et al. 2025; Villaseñor et al. 2025; Bodensteiner et al. 2025; Sana et al. 2025). Therefore, other processes should be considered to explain the nitrogen enhancement, such as binary interaction in the history of the star or the potential existence of a currently undetected companion.

Fig. 7 shows the ratio N/C versus N/O. Following the analytical solution of Maeder et al. (2014), the upper and lower CNO limits (dashed black lines) were calculated using the baseline CNO abundance averages of the SMC from Vink et al. (2023). The majority of our sample falls between the two boundaries and agrees with the expected yield of elements processed by the CNO cycle. The exceptions are AzV 324 and AzV 343, for which we obtained the oxygen abundance by fitting the O I $\lambda\lambda\lambda$7772–7774–7775 multiplet, due to the absence of any other oxygen lines in the optical range. We found that a satisfactory fit to this complex line requires a reduction in the oxygen mass fraction in the model by a factor of four, which explains the high N/O ratios in Fig. 7 for these objects. As is explained in Paper XIII, the O I $\lambda\lambda\lambda$7772–7774–7775 multiplet is extremely sensitive to $T_{\rm eff}$ variations at this range; therefore, the oxygen content obtained by fitting those lines is highly uncertain.

Table 7. Slopes, x, and vertical offsets, $\log D_0$, of Equation (5) of this study and from Paper XIII.

Galaxy	x	$\log D_0$	Sp. T.	Lum. Cl.	num. stars
SMC	1.73 ± 1.00	17.8 ± 5.62	O9-B3	I	9
LMC	1.39 ± 0.54	20.42 ± 3.04	O9-B3	I	14

Our sample has two stars (AzV 469 and AzV 327) in common with Martins et al. (2024), who employed CMFGEN to obtain the chemical abundances of a sample of SMC and LMC O stars using spectroscopy from ULLYSES and XShootU. We find that our obtained ϵ_N for these stars agrees within 0.1 dex with their derived nitrogen abundances, whereas carbon and oxygen do not agree so well, though they match within the quoted uncertainties.

We find that the total CNO mass fraction is conserved for most of our sample, except AzV 469, AzV 372, and AzV 215. In the case of these stars, enhanced nitrogen abundances were required to obtain a satisfactory match to the diagnostic lines, and oxygen mass fractions slightly larger than baseline were also required to obtain satisfactory fits for oxygen lines. This explains the implausibly large ratio of cumulative CNO mass fraction to the cumulative solar CNO mass fraction, $\Sigma\mathrm{CNO}/\Sigma\mathrm{CNO}_\odot$. We use these example as a reminder of the large uncertainties associated with the determination of abundances in supergiants from our approach, which are in part due to the sensitivity of the ionisation structure of CNO lines to variations in $T_{\rm eff}$ and $\log g$, but also the fixed micro-turbulent velocity, and the extent of the atomic model adopted in the calculation (number of important levels and superlevels), and the incompleteness of the atomic data.

5. Discussion

5.1. Metallicity effect

Fig. 8 shows the modified wind momentum, which was introduced by Kudritzki et al. (1999) as $D_{\rm mom} = \dot{M} v_\infty \sqrt{R_*/R_\odot}$, as a function of $L_{\rm bol}$. We fitted our derived values using the relation

$$\log D_{\rm mom}^{\rm SMC} = \log D_0 + x \log \frac{L_{\rm bol}}{L_\odot}. \tag{5}$$

In Fig. 8, solid lines are fits to the stars (circles) that show both P Cygni profiles in the UV and Hα in emission, making their determined wind parameters the most reliable. We can see that including stars with Hα in absorption (triangles) in the linear fit slightly changes the slope of the fit for the LMC sample from Paper XII (dash-dotted green line). Doing the same for our SMC sample decreases the vertical offset of the fit (dash-dotted yellow line), albeit very slightly.

In Table 7, we present the best fitting parameters of Equation (5) (slopes, x, and offsets, $\log D_0$). Comparing the $D_{\rm mom}$

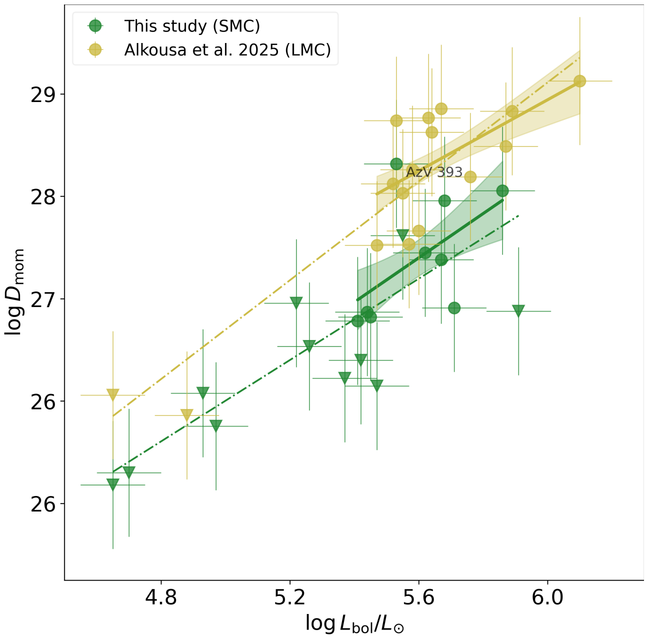

Fig. 8. $D_{\rm mom}$ vs $logL_{\rm bol}$. The green symbols represent the SMC sample. The yellow symbols represent the LMC sample from Paper XIII. Circles indicate stars with reliable UV and optical wind diagnostics. Triangles indicate upper limits. Solid lines are fits to the circles. Dash-dotted lines are fits for the entire sample.

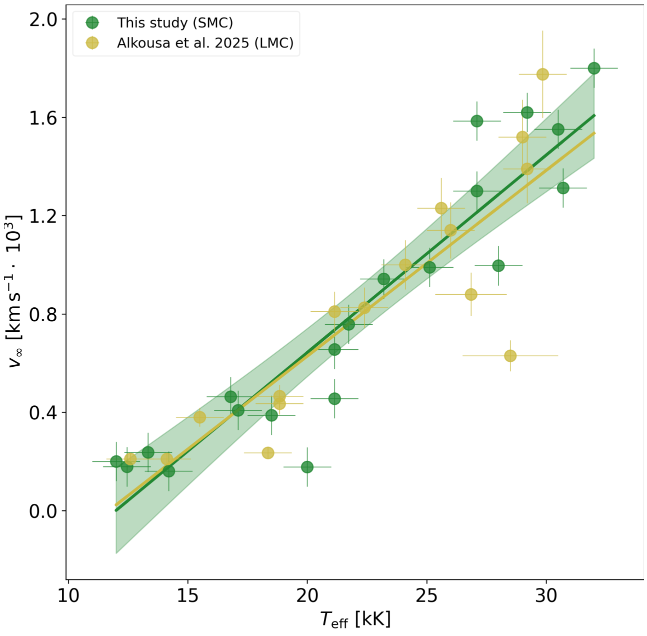

Fig. 9. $\varv_\infty$ vs $T_{\rm eff}$. The symbol and colour encoding are the same as in Fig. 8.

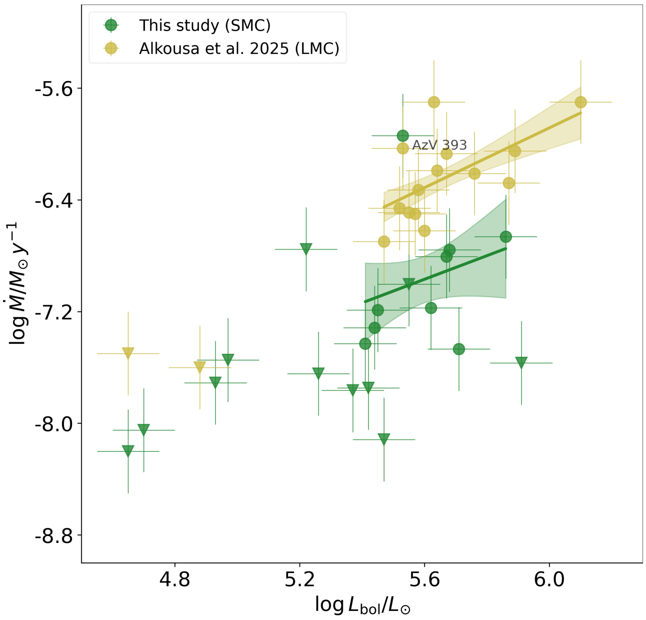

Fig. 10. log $\dot{M}$ vs log $L_{\rm bol}$. The symbol and colour encoding are the same as in Fig. 8.

Table 8. Fitting parameter of Equation (6).

Parameter	This study	Backs et al. (2024)
a	1.16 ± 0.48	0.64
b	−0.75 ± 1.14	−2.84
c	1.38 ± 4.03	0.71
d	29.17 ± 6.39	29.27

of the current SMC sample to the LMC sample analysed in Paper XIII, we find that the slope of the SMC is slightly steeper than the LMC, albeit quite similar. We also find a large difference in the intercepts between the two samples, which can be attributed to the Z dependence of wind properties.

In Figure 9, we show $\varv_\infty$ as a function of $T_{\rm eff}$ of the present study compared to the results from Paper XIII. Figure 10 shows log $\dot{M}$ vs log $L_{\rm bol}$ from this study compared to Paper XIII. $\varv_\infty$ does not show signs of Z dependence, whereas log $\dot{M}$ shows a clear offset between the two samples, indicating a strong Z dependence. Therefore, we can assume that the Z dependence of $D_{\rm mom}$ is dominated by the Z dependence of $\dot{M}$.

In parallel with our study, Verhamme et al. (2025) have recently undertaken an analysis of ULLYSES/XShootU SMC B supergiants. To investigate the effect of metallicity, they compare their analysis to an earlier study of LMC B supergiants (Verhamme et al. 2024). Despite our overlapping samples, they arrived at different conclusions, which is discussed further in Appendix B.

Following Krtička & Kubát (2018) and Backs et al. (2024), we obtained an equation for the Z-dependent log $D_{\rm mom}$ of the form

$$\log D_{\rm mom} = \left(a + b\log\frac{Z}{Z_\odot}\right)\log\frac{L_{\rm bol}}{10^6 L_\odot} + c\log\frac{Z}{Z_\odot} + d, \qquad (6)$$

where from Equation (5) $x = a + b\log\frac{Z}{Z_\odot}$, $\log D_0 = c\log\frac{Z}{Z_\odot} + d$, and a, b, c, and d are fitting parameters. The results of the fitting are presented in Table 8, assuming that $Z_{\rm LMC} = 0.5Z_\odot$ and $Z_{\rm SMC} = 0.2Z_\odot$. We also include values from Backs et al. (2024) in Table 8.

5.2. Bi-stability jump

In Fig. 11, we present our derived log $\dot{M}$ in terms of $T_{\rm eff}$. This confirms that AzV 393 possesses much higher $\dot{M}$, not just compared to objects with similar $T_{\rm eff}$, but even compared to the hotter OB supergiants in our sample. We do not find any sign of a large increase in $\dot{M}$ around 25–21 kK, which could be attributed to the

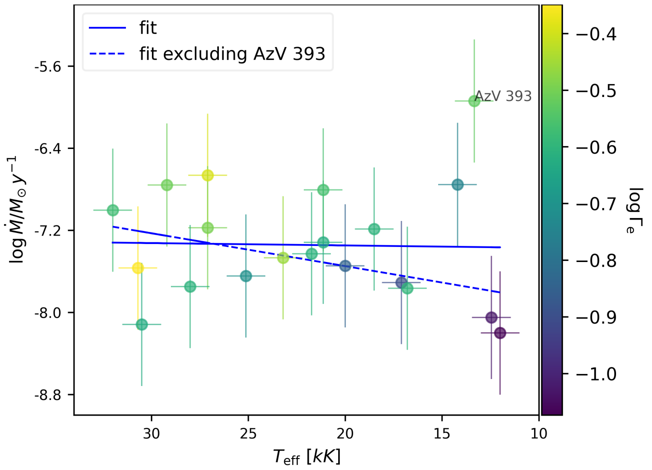

Fig. 11. $\log \dot{M}$ versus $T_{\rm eff}$. The solid blue line is a simple linear fit to the entire sample. The colour gradient correlates with the value of Γ_e.

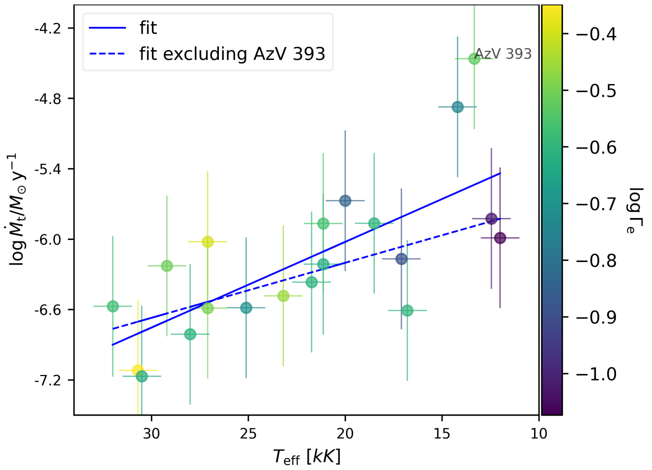

Fig. 12. $\log \dot{M}_{\rm t}$ versus $T_{\rm eff}$. The symbol and colour encoding are the same as in Fig. 11.

bi-stability jump. Using a simple linear regression, we find that $\log \dot{M}$ is constant with $T_{\rm eff}$ (solid blue line). Excluding the hypergiant AzV 393 from the fit (dashed blue line), we find that $\log \dot{M}$ decreases with $T_{\rm eff}$.

To investigate the effect of luminosity, we calculated the transformed mass-loss rate, which is defined as

$$\dot{M}_{\rm t} = \dot{M} \cdot f_{\rm vol,\infty}^{-1/2} \cdot (10^3 {\rm km\,s^{-1}}/v_\infty) \cdot (10^6 L_\odot/L_{\rm bol})^{3/4}. \tag{7}$$

In Fig. 12, we compare $\log \dot{M}_{\rm t}$ to $T_{\rm eff}$. We find that when including or excluding AzV 393 in the linear fit, $\log \dot{M}_{\rm t}$ increases with temperature. This is in contrast to the results of Bernini-Peron et al. (2024), which hint at a constant behaviour of the mass-loss rate with temperature. The reason for this trend could be our comparably low values of $f_{\rm vol,\infty} < 0.2$ (i.e. a high degree of clumping in the winds), which lowers the mass-loss rates required to obtain a satisfactory fit to Hα and to the UV P Cygni profiles.

In Fig. 13, we present the ratio v_∞ to the escape velocity $v_{\rm esc}$ as a function of $T_{\rm eff}$, which was calculated using $M_{\rm evo}$. From our results, we derive a relation of

$$v_\infty/v_{\rm esc} = 4.6(\pm0.9)\log(T_{\rm eff}/{\rm K}) - 18.3(\pm3.8), \tag{8}$$

where $v_{\rm esc} = \sqrt{2GM(1-\Gamma_{\rm e})/R_*}$, and $\Gamma_{\rm e}$ is the Eddington parameter, which was calculated using $M_{\rm evo}$.

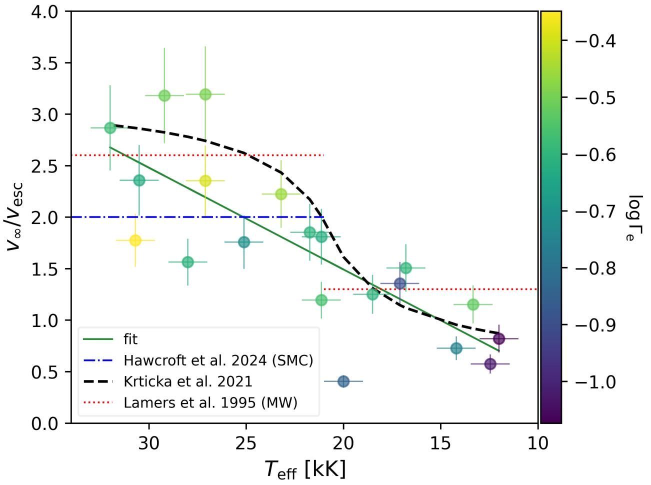

Fig. 13. Ratio ($v_\infty/v_{\rm esc}$) as a function of temperature. The solid green line represents the linear fit to our sample. The dashed black line is the relation presented in Krtička et al. (2021). The dotted red lines represent the ratios from Lamers et al. (1995). The colour gradient correlates with the value of Γ_e.

We do not notice any drastic decrease in $v_\infty/v_{\rm esc}$ below $T_{\rm eff}$ = 25-21 kK, indicative of the theorised bi-stability jump. We find that $v_\infty/v_{\rm esc}$ decreases monotonically with $T_{\rm eff}$. These results show a lack of evidence for the existence of the bi-stability jump, which is similar to the findings of Paper XIII, as well as the findings of de Burgos et al. (2024a) in the MW, Bernini-Peron et al. (2024) in the SMC, and Verhamme et al. (2024) in the LMC. In Appendix C, we include some additional discussion on the bi-stability jump.

5.3. Implications for the population of blue supergiants

Recalling the HRD in Fig. 1, the shaded region is defined by the observed HD limit (Humphreys & Davidson 1979, 1994) in the SMC, which has a value of $\log L_{\rm bol}/L_\odot \approx 5.5$ (Davies et al. 2018). The diagonal blue edge of this region is inferred from the distribution of known luminous blue variables (LBVs) and LBV candidates on the HRD (Smith et al. 2004).

The HD limit suggests that the most massive stars with luminosities higher than $\log L_{\rm bol}/L_\odot \approx 5.5$ remain as blue supergiants, and end their lives as blue hypergiants and classical Wolf-Rayet (WR) stars, rather than evolving into luminous red supergiants. This means that, at least in theory, they should have sufficiently high mass-loss rates to shed their hydrogen-rich atmospheres and proceed to a classical WR phase. The existence of a considerable non-binary population of WRs in the SMC (e.g. Hainich et al. 2015; Schootemeijer et al. 2024) with high luminosity, for which Shenar et al. (2020) finds a non-binary fraction of ≈60-70%, in addition to a lower limit on WR luminosity of $\log L_{\rm bol}/L_\odot = 5.6$, which is comparable to the uppermost part of our sample and could, in principle, be seen as an argument for a self-stripping evolutionary scenario via extreme LBV eruptions.

However, aligning this evolutionary scenario with the mass-loss rates obtained in studies of blue supergiants in the SMC (This study, Bernini-Peron et al. 2024; Trundle & Lennon 2005; Trundle et al. 2004) poses a challenge for explaining the formation of WR stars from radiation-driven mass loss alone in the single-star regime. By way of example, AzV 242 has an evolutionary mass of $M_{\rm evo} = 37.89^{+4.01}_{-3.94}\ M_{\odot}$, a luminosity of $\log L_{\rm bol}/L_{\odot} = 5.71 \pm 0.1$, and a mass-loss rate of $\log \dot{M}/M_{\odot}\,{\rm yr}^{-1} = -7.47 \pm 0.4$. AzV 242 closely corresponds to the minimum initial mass of WR stars in the SMC (Shenar et al. 2020), yet the mass-loss rate of this supergiant is far too low to result in the stripping of the outer hydrogen-rich layers within its remaining ~0.5 Myr lifetime.

The low current mass-loss rates, together with the observed properties of WR populations and the lack of luminous red supergiants in the SMC, leads to the following conclusion: to form a WR star via single-star evolution, luminous blue supergiants would need to lose copious amounts of mass during an LBV giant eruption (Smith 2017; Jiang et al. 2018). This is supported by recent work from Pauli et al. (2026), who were able to replicate the observed properties of the WR and RSG populations – including the low-luminosity single WRs – in the SMC by incorporating LBV-like Eddington-limit induced mass loss in evolutionary models. It is also probable that binarity, mass transfer via Roche lobe overflow, and common envelope evolution play a significant role in shaping the WR population (Schootemeijer & Langer 2018).

6. Summary and conclusions

We have completed a spectroscopic analysis of 20 late-O and B SMC supergiants, which employed CMFGEN (Hillier & Miller 1998), using the UV (ULLYSES) and optical (XShootU) spectral ranges. We obtained stellar and wind parameters of the stars in our sample. By comparing our results to those of Alkousa et al. (2025) for the LMC, we find a clear Z dependence in wind momentum, which is shown in Fig. 8. We derived the wind momentum-luminosity relation presented in Equation (6). We also found a clear Z dependence in mass-loss rates, but did not find similar Z dependence in the terminal wind velocities.

We compared our derived mass-loss rates to predictions from various numerical recipes Vink & Sander (2021); Björklund et al. (2023); Krtička et al. (2024). We found that the values of the numerical recipes differ from our mass-loss rates, with the recipe from Krtička et al. (2024) producing the values most closely aligned with ours, yet still showing a different trend with temperature.

We also compared our results to literature values of the same stars (Trundle et al. 2004; Trundle & Lennon 2005; Backs et al. 2024; Bernini-Peron et al. 2024; Bestenlehner et al. 2025). On the one hand, we find that the effective temperature, surface gravity, and luminosity generally agree with previous studies with modest variance. However, our derived mass-loss rates do not match previous estimates, with our values being generally lower than those previously obtained by previous studies.

We do not find any sign of the theorised bi-stability jump. This is similar to the findings of de Burgos et al. (2024a), Bernini-Peron et al. (2024), Verhamme et al. (2024), and Alkousa et al. (2025). This means that within the current framework of radiative transfer codes used for modelling OB stars, the dramatic increase in mass loss at $T_{\rm eff} = 25$–21 kK that is associated with the theorised bi-stability jump is not empirically supported.

We also explored the evolutionary history of the stars within our sample. We employed an updated Bayesian inference method (V. Bronner et al., in prep.) similar to BONNSAI (Schneider et al. 2014) to obtain the evolutionary masses and ages using the rotating single-star evolutionary tracks of Brott et al. (2011). Evolutionary masses typically exceed spectroscopic masses, with 40% of our sample showing a mass discrepancy.

Finally, we emphasise that mass-loss rates of supergiants exceeding the HD limit of $\log L_{\rm bol}/L_{\odot} = 5.5$ (Davies et al. 2018) are far too low to be able to strip the supergiants of their hydrogen-rich outer layers. Consequently, the high fraction of single WR stars observed in the SMC (Shenar et al. 2020) cannot be explained by the classical single star evolutionary regime, unless the supergiant is capable of losing an enormous amount of mass within its very short remaining lifespan. This possibly means that an intermediate LBV phase that is accompanied by extreme episodic eruptions and mass loss is required for the star to proceed into a WR phase.

In the next installment of this series of papers, we plan to analyse a similar sample of Galactic blue supergiants using the same methods as are presented in Paper XIII. This will allow us to derive a mass-loss rate recipe for supergiants, which avoids differences introduced by utilising various analysis techniques and codes.

Data availability

The supplementary online material can be found on Zenodo[1]. Appendix G includes comments on diagnostic-line fits for all the targets in our sample. Additionally, SED fits, diagnostic-line fits, and overall UV and optical spectral fits can be found in Appendix H, I, and Appendix J, respectively.

Acknowledgements. TA would like to thank the Science and Technology Facilities Council (STFC) for financial support through the STFC scholarship ST/X508743/1. RK acknowledges financial support via the Heisenberg Research Grant funded by the Deutsche Forschungsgemeinschaft (DFG, German Research Foundation) under grant no. KU 2849/9, project no. 445783058. F.N., acknowledges support by PID2022-137779OB-C41 funded by MCIN/AEI/10.13039/501100011033 by "ERDF A way of making Europe". AACS and MBP are supported by the German *Deutsche Forschungsgemeinschaft, DFG* in the form of an Emmy Noether Research Group – Project-ID 445674056 (SA4064/1-1, PI Sander). This project was co-funded by the European Union (Project 101183150 – OCEANS).This study was made possible through the Director's discretionary ULLYSES survey, which was implemented by a Space Telescope Science Institute (STScI) team led by Julia Roman-Duval. Based on observations made with ESO telescopes at the Paranal observatory under programme ID 106.211Z.001 and observations obtained with the NASA/ESA Hubble Space Telescope, retrieved from the Mikulski Archive for Space Telescopes (MAST) at the STScI. STScI is operated by the Association of Universities for Research in Astronomy, Inc. under NASA contract NAS 5-26555. We also thank John Hillier for developing CMFGEN, Nidia Morrell for obtaining and reducing MIKE data in addition to her feedback on this paper, and Vincent Bronner for facilitating the use of his Bayesian inference technique. This research has used the SIMBAD database, operated at CDS, Strasbourg, France. We would like to thank the referee for their critical and insightful comments.

References

Abbott, D. C. 1982, ApJ, 259, 282
Alkousa, T., Crowther, P. A., Bestenlehner, J. M., et al. 2025, A&A, 699, A314
Anderson, L. S. 1985, ApJ, 298, 848
Anderson, L. S. 1989, ApJ, 339, 558
Ardeberg, A. 1980, A&AS, 42, 1
Ardeberg, A., & Maurice, E. 1977, A&AS, 30, 261
Azzopardi, M., Vigneau, J., & Macquet, M. 1975, A&AS, 22, 285
Backs, F., Brands, S. A., de Koter, A., et al. 2024, A&A, 692, A88
Beckman, J. E., & Crivellari, L. 1985, Science, 230, 835
Bernini-Peron, M., Sander, A. A. C., Ramachandran, V., et al. 2024, A&A, 692, A89
Bestenlehner, J. M., Enßlin, T., Bergemann, M., et al. 2024, MNRAS, 528, 6735
Bestenlehner, J. M., Crowther, P. A., Hawcroft, C., et al. 2025, A&A, 695, A198
Björklund, R., Sundqvist, J. O., Singh, S. M., Puls, J., & Najarro, F. 2023, A&A, 676, A109

---

[1] `https://doi.org/10.5281/zenodo.18416382`

Bodensteiner, J., Shenar, T., Sana, H., et al. 2025, A&A, 698, A38
Brands, S. A., Backs, F., de Koter, A., et al. 2025, A&A, 697, A54
Bresolin, F., Kudritzki, R.-P., & Urbaneja, M. A. 2022, ApJ, 940, 32
Britavskiy, N., Mahy, L., Lennon, D. J., et al. 2025, A&A, 698, A40
Brott, I., de Mink, S. E., Cantiello, M., et al. 2011, A&A, 530, A115
Castor, J. I., Abbott, D. C., & Klein, R. I. 1975, ApJ, 195, 157
Castor, J. I., & Lamers, H. J. G. L. M. 1979, ApJS, 39, 481
Cioni, M. R., Clementini, G., Girardi, L., et al. 2011, The Messenger, 144, 25
Conti, P. S., & Ebbets, D. 1977, ApJ, 213, 438
Crowther, P. A. 2024, in IAU Symposium, 361, IAU Symposium, eds. J. Mackey, J. S. Vink, & N. St-Louis, 15
Crowther, P. A., Lennon, D. J., & Walborn, N. R. 2006, A&A, 446, 279
Cutri, R. M., Skrutskie, M. F., van Dyk, S., et al. 2003, VizieR On-line Data Catalog: II/246. Originally published in: University of Massachusetts and Infrared Processing and Analysis Center, (IPAC/California Institute of Technology)
Cutri, R. M., Skrutskie, M. F., van Dyk, S., et al. 2012, VizieR On-line Data Catalog: II/281. Originally published in: 2012yCat.2281....0C
Danforth, C. W., Howk, J. C., Fullerton, A. W., Blair, W. P., & Sembach, K. R. 2002, ApJS, 139, 81
Davies, B., Crowther, P. A., & Beasor, E. R. 2018, MNRAS, 478, 3138
de Burgos, A., Keszthelyi, Z., Simón-Díaz, S., & Urbaneja, M. A. 2024a, A&A, 687, L16
de Burgos, A., Simón-Díaz, S., Urbaneja, M. A., & Puls, J. 2024b, A&A, 687, A228
de Mink, S. E., Langer, N., Izzard, R. G., Sana, H., & de Koter, A. 2013, ApJ, 764, 166
Dufton, P. L., Ryans, R. S. I., Simón-Díaz, S., Trundle, C., & Lennon, D. J. 2006, A&A, 451, 603
Eddington, A. S. 1926, The Internal Constitution of the Stars
Evans, C. J., Lennon, D. J., Walborn, N. R., Trundle, C., & Rix, S. A. 2004, PASP, 116, 909
Fitzpatrick, E. L., & Massa, D. 1990, ApJS, 72, 163
Fouesneau, M. 2025, pyphot: A tool for computing photometry from spectra, `https://github.com/mfouesneau/pyphot`
Geen, S., Agrawal, P., Crowther, P. A., et al. 2023, PASP, 135, 021001
Gordon, K. D., Clayton, G. C., Misselt, K. A., Landolt, A. U., & Wolff, M. J. 2003, ApJ, 594, 279
Graczyk, D., Pietrzyński, G., Thompson, I. B., et al. 2020, ApJ, 904, 13
Green, J. C., Froning, C. S., Osterman, S., et al. 2012, ApJ, 744, 60
Hainich, R., Pasemann, D., Todt, H., et al. 2015, A&A, 581, A21
Hardorp, J., & Scholz, M. 1970, ApJS, 19, 193
Hawcroft, C., Mahy, L., Sana, H., et al. 2024a, A&A, 690, A126
Hawcroft, C., Sana, H., Mahy, L., et al. 2024b, A&A, 688, A105
Herrero, A., Kudritzki, R. P., Vilchez, J. M., et al. 1992, A&A, 261, 209
Hillier, D. J. 1990, A&A, 231, 116
Hillier, D. J. 1996, in Liege International Astrophysical Colloquia, 33, Liege International Astrophysical Colloquia, eds. J. M. Vreux, A. Detal, D. Fraipont-Caro, E. Gosset, & G. Rauw, 509
Hillier, D. J. 1997, in IAU Symposium, 189, IAU Symposium, eds. T. R. Bedding, A. J. Booth, & J. Davis, 209
Hillier, D. J., & Miller, D. L. 1998, ApJ, 496, 407
Hillier, D. J., & Miller, D. L. 1999, ApJ, 519, 354
Holgado, G., Simón-Díaz, S., Herrero, A., & Barbá, R. H. 2022, A&A, 665, A150
Humphreys, R. M., & Davidson, K. 1979, ApJ, 232, 409
Humphreys, R. M., & Davidson, K. 1994, PASP, 106, 1025
Hunter, I., Brott, I., Lennon, D. J., et al. 2008, ApJ, 676, L29
Jiang, Y.-F., Cantiello, M., Bildsten, L., et al. 2018, Nature, 561, 498
Krtička, J., & Kubát, J. 2018, A&A, 612, A20
Krtička, J., Kubát, J., & Krtičková, I. 2021, A&A, 647, A28
Krtička, J., Kubát, J., & Krtičková, I. 2024, A&A, 681, A29
Kudritzki, R. P., Pauldrach, A., & Puls, J. 1987, A&A, 173, 293
Kudritzki, R. P., Puls, J., Lennon, D. J., et al. 1999, A&A, 350, 970
Kudritzki, R. P., Bresolin, F., & Przybilla, N. 2003, ApJ, 582, L83
Kudritzki, R.-P., Urbaneja, M. A., Bresolin, F., et al. 2008, ApJ, 681, 269
Kudritzki, R.-P., Urbaneja, M. A., Bresolin, F., et al. 2024, ApJ, 977, 217
Lamers, H. J. G. L. M., Snow, T. P., & Lindholm, D. M. 1995, ApJ, 455, 269
Langer, N. 2012, Annu. Rev. Astron. Astrophys., 50, 107
Lanz, T., & Hubeny, I. 2007, ApJS, 169, 83
Leitherer, C., Robert, C., & Drissen, L. 1992, ApJ, 401, 596
Lennon, D. J., Dufton, P. L., & Fitzsimmons, A. 1992, A&AS, 94, 569
Lucy, L. B., & Solomon, P. M. 1970, ApJ, 159, 879
Maeder, A., Przybilla, N., Nieva, M.-F., et al. 2014, A&A, 565, A39
Marcolino, W. L. F., Bouret, J. C., Rocha-Pinto, H. J., Bernini-Peron, M., & Vink, J. S. 2022, MNRAS, 511, 5104
Martins, F. 2011, Bull. Soc. Roy. Sci. Liege, 80, 29
Martins, F., Bouret, J. C., Hillier, D. J., et al. 2024, A&A, 689, A31
Massa, D. L., Prinja, R. K., & Fullerton, A. W. 2008, in Clumping in Hot-Star Winds, eds. W.-R. Hamann, A. Feldmeier, & L. M. Oskinova, 147
Massey, P. 2002, ApJS, 141, 81
McErlean, N. D., Lennon, D. J., & Dufton, P. L. 1998, A&A, 329, 613
McErlean, N. D., Lennon, D. J., & Dufton, P. L. 1999, A&A, 349, 553
Mokiem, M. R., de Koter, A., Evans, C. J., et al. 2006, A&A, 456, 1131
Mokiem, M. R., de Koter, A., Vink, J. S., et al. 2007, A&A, 473, 603
Moos, H. W., Cash, W. C., Cowie, L. L., et al. 2000, ApJ, 538, L1
Nieva, M. F. 2013, A&A, 550, A26
Pauli, D., Oskinova, L. M., Hamann, W. R., et al. 2025, A&A, 697, A114
Pauli, D., Langer, N., Schootemeijer, A., et al. 2026, A&A, 707, A11
Prinja, R. K., & Crowther, P. A. 1998, MNRAS, 300, 828
Prinja, R. K., Barlow, M. J., & Howarth, I. D. 1990, ApJ, 361, 607
Puls, J., Kudritzki, R. P., Herrero, A., et al. 1996, A&A, 305, 171
Puls, J., Urbaneja, M. A., Venero, R., et al. 2005, A&A, 435, 669
Puls, J., Vink, J. S., & Najarro, F. 2008, A&A Rev., 16, 209
Ramachandran, V., Hamann, W. R., Oskinova, L. M., et al. 2019, A&A, 625, A104
Ramírez-Agudelo, O. H., Simón-Díaz, S., Sana, H., et al. 2013, A&A, 560, A29
Rivero González, J. G., Puls, J., & Najarro, F. 2011, A&A, 536, A58
Roman-Duval, J., Fischer, W. J., Fullerton, A. W., et al. 2025, ApJ, 985, 109
Russell, S. C., & Dopita, M. A. 1990, ApJS, 74, 93
Sana, H., Tramper, F., Abdul-Masih, M., et al. 2024, A&A, 688, A104
Sana, H., Shenar, T., Bodensteiner, J., et al. 2025, Nat. Astron., 9, 1337
Sander, A. A. C., Bouret, J. C., Bernini-Peron, M., et al. 2024, A&A, 689, A30
Schmutz, W., Hamann, W. R., & Wessolowski, U. 1989, A&A, 210, 236
Schneider, F. R. N., Langer, N., de Koter, A., et al. 2014, A&A, 570, A66
Schootemeijer, A., & Langer, N. 2018, A&A, 611, A75
Schootemeijer, A., Shenar, T., Langer, N., et al. 2024, A&A, 689, A157
Scowcroft, V., Freedman, W. L., Madore, B. F., et al. 2016, ApJ, 816, 49
Searle, S. C., Prinja, R. K., Massa, D., & Ryans, R. 2008, A&A, 481, 777
Shenar, T., Gilkis, A., Vink, J. S., Sana, H., & Sander, A. A. C. 2020, A&A, 634, A79
Shenar, T., Bodensteiner, J., Sana, H., et al. 2024, A&A, 690, A289
Simón-Díaz, S., & Herrero, A. 2014, A&A, 562, A135
Simón-Díaz, S., Herrero, A., Uytterhoeven, K., et al. 2010, ApJ, 720, L174
Skrutskie, M. F., Cutri, R. M., Stiening, R., et al. 2006, AJ, 131, 1163
Slettebak, A. 1956, ApJ, 124, 173
Smartt, S. J. 2009, ARA&A, 47, 63
Smith, N. 2014, ARA&A, 52, 487
Smith, N. 2017, Philos. Trans. Roy. Soc. Lond. Ser. A, 375, 20160268
Smith, N., Vink, J. S., & de Koter, A. 2004, ApJ, 615, 475
Sundqvist, J. O., Debnath, D., Backs, F., et al. 2025, A&A, 703, A284
Trundle, C., & Lennon, D. J. 2005, A&A, 434, 677
Trundle, C., Lennon, D. J., Puls, J., & Dufton, P. L. 2004, A&A, 417, 217
Trundle, C., Dufton, P. L., Hunter, I., et al. 2007, 471, 625
Urbaneja, M. A., Herrero, A., Bresolin, F., et al. 2005a, ApJ, 622, 862
Urbaneja, M. A., Herrero, A., Kudritzki, R. P., et al. 2005b, ApJ, 635, 311
Urbaneja, M. A., Kudritzki, R. P., Gieren, W., et al. 2017, AJ, 154, 102
Verhamme, O., Sundqvist, J., de Koter, A., et al. 2024, A&A, 692, A91
Verhamme, O., Sundqvist, J., & XShootU Collaboration. 2025, A&A
Vernet, J., Dekker, H., D'Odorico, S., et al. 2011, A&A, 536, A105
Villaseñor, J. I., Sana, H., Mahy, L., et al. 2025, A&A, 698, A41
Vink, J. S., & Sander, A. A. C. 2021, MNRAS, 504, 2051
Vink, J. S., de Koter, A., & Lamers, H. J. G. L. M. 1999, A&A, 350, 181
Vink, J. S., de Koter, A., & Lamers, H. J. G. L. M. 2001, A&A, 369, 574
Vink, J. S., Mehner, A., Crowther, P. A., et al. 2023, A&A, 675, A154
Walborn, N. R., Lennon, D. J., Heap, S. R., et al. 2000, PASP, 112, 1243
Walborn, N. R., Fullerton, A. W., Crowther, P. A., et al. 2002, ApJS, 141, 443
Woodgate, B. E., Kimble, R. A., Bowers, C. W., et al. 1998, PASP, 110, 1183

Appendix A: Main results table

Table A.1: Derived stellar parameters based on the best fitting CMFGEN model.

Star	$T_{\rm eff}$	Diag.	$\log g_c$	R_*	$\log L_{\rm bol}$	A_V	$M_{\rm V}$	$BC_{\rm V}$	$\upsilon_{\rm rad}$	$\upsilon_{\rm rot} \sin i$	$M_{\rm spec}$	$\Gamma_{\rm e}^{\rm spec}$	M_{init}	$M_{\rm evo}$	Age	$\Gamma_{\rm e}^{\rm evo}$
	kK		cm s^{-2}	$R_\odot$	$L_\odot$	mag	mag	mag	km s^{-1}	km s^{-1}	$M_\odot$		$M_\odot$	$M_\odot$	Myr	
AzV 469	32.0	He I – He II	3.30	19 ± 1	5.55	0.27	−6.11	−3.03	185	55	27.6 ± 3.9	0.29 ± 0.06	$32.24^{+7.60}_{-6.68}$	$29.89^{+9.21}_{-6.12}$	$4.34^{+1.52}_{-0.63}$	$0.27^{+0.08}_{-0.06}$
AzV 372	29.2	He I – He II	3.00	27 ± 2	5.68	0.28	−6.65	−2.80	251	100	28.1 ± 4.3	0.38 ± 0.08	$37.20^{+5.74}_{-5.88}$	$34.73^{+7.15}_{-5.52}$	$4.86^{+0.32}_{-1.11}$	$0.31^{+0.06}_{-0.05}$
AzV 456	30.7	He I – He II	3.35	32 ± 2	5.91	0.97	−7.10	−2.94	141	55	83.4 ± 11.8	0.25 ± 0.05	$50.34^{+5.75}_{-5.29}$	$46.77^{+6.39}_{-3.65}$	$3.26^{+0.21}_{-0.33}$	$0.45^{+0.06}_{-0.04}$
AzV 327	30.5	He I – He II	3.32	19 ± 1	5.47	0.09	−6.02	−2.92	179	55	29.1 ± 4.1	0.24 ± 0.05	$30.14^{+3.78}_{-5.13}$	$29.47^{+3.35}_{-5.16}$	$4.90^{+0.65}_{-0.76}$	$0.23^{+0.03}_{-0.04}$
AzV 235	27.1	Si III – Si IV	2.98	39 ± 3	5.86	0.52	−7.28	−2.64	165	60	52.7 ± 8.4	0.35 ± 0.08	$48.08^{+5.20}_{-6.51}$	$46.13^{+4.22}_{-6.48}$	$3.46^{+0.38}_{-0.30}$	$0.40^{+0.04}_{-0.06}$
AzV 215	27.1	Si III – Si IV	2.95	29 ± 2	5.62	0.42	−6.69	−2.63	165	60	28.4 ± 4.5	0.38 ± 0.08	$34.74^{+4.80}_{-3.70}$	$33.44^{+4.75}_{-3.16}$	$4.34^{+0.52}_{-0.47}$	$0.32^{+0.05}_{-0.03}$
AzV 104	28.0	Si III – Si IV	3.25	22 ± 2	5.42	0.28	−6.07	−2.72	140	65	31.2 ± 4.6	0.22 ± 0.05	$27.96^{+3.08}_{-2.71}$	$27.48^{+2.80}_{-2.71}$	$5.22^{+0.57}_{-0.49}$	$0.25^{+0.03}_{-0.03}$
AzV 410	25.1	Si III – Si IV	3.10	23 ± 2	5.26	0.19	−5.94	−2.47	185	85	24.2 ± 3.8	0.19 ± 0.04	$23.28^{+2.45}_{-2.22}$	$23.17^{+2.15}_{-2.43}$	$6.43^{+0.89}_{-0.67}$	$0.20^{+0.02}_{-0.02}$
AzV 242	23.2	Si III – Si IV	2.65	44 ± 4	5.71	0.35	−7.25	−2.25	177	55	32.7 ± 5.9	0.40 ± 0.09	$39.47^{+4.69}_{-4.18}$	$37.89^{+4.01}_{-3.94}$	$4.15^{+0.41}_{-0.34}$	$0.35^{+0.04}_{-0.04}$
AzV 96	21.7	Si III – Si IV	2.65	36 ± 3	5.41	0.30	−6.67	−2.12	158	50	21.3 ± 3.9	0.31 ± 0.07	$27.78^{+2.21}_{-3.74}$	$26.88^{+2.14}_{-3.35}$	$5.87^{+0.64}_{-0.69}$	$0.25^{+0.02}_{-0.03}$
AzV 264	21.1	Si III – Si IV	2.50	39 ± 4	5.44	0.23	−6.82	−2.04	131	45	18.1 ± 3.5	0.36 ± 0.08	$28.40^{+3.85}_{-4.17}$	$27.31^{+3.64}_{-3.68}$	$5.89^{+0.58}_{-1.02}$	$0.24^{+0.03}_{-0.03}$
AzV 175	20.0	Si III – Si IV	2.80	25 ± 3	4.97	0.31	−5.74	−1.93	175	30	15.0 ± 2.7	0.16 ± 0.04	$17.11^{+1.80}_{-1.31}$	$16.69^{+2.07}_{-1.01}$	$9.30^{+1.22}_{-0.99}$	$0.14^{+0.02}_{-0.01}$
Sk 191	21.1	Si III – Si IV	2.45	51 ± 5	5.67	0.52	−7.62	−2.06	127	65	27.9 ± 5.4	0.4 ± 0.09	$43.04^{+3.56}_{-3.14}$	$40.81^{+3.13}_{-2.93}$	$3.98^{+0.28}_{-0.23}$	$0.27^{+0.02}_{-0.02}$
AzV 18	18.5	Si II – Si III	2.25	52 ± 6	5.45	0.66	−7.16	−1.73	150	50	18.0 ± 3.9	0.37 ± 0.09	$27.50^{+3.67}_{-3.03}$	$27.21^{+2.88}_{-3.47}$	$5.57^{+0.80}_{-0.62}$	$0.25^{+0.03}_{-0.03}$
NGC330-ELS-04	17.1	Si II – Si III	2.35	33 ± 4	4.93	0.37	−6.00	−1.57	158	35	9.2 ± 2.0	0.46 ± 0.10	$16.58^{+1.64}_{-1.31}$	$16.49^{+1.59}_{-1.32}$	$9.79^{+1.26}_{-1.10}$	$0.13^{+0.01}_{-0.01}$
AzV 187	16.8	Si II – Si III	2.20	57 ± 7	5.37	0.25	−7.15	−1.54	139	40	19.4 ± 4.4	0.22 ± 0.05	$24.51^{+4.07}_{-3.72}$	$24.01^{+4.41}_{-4.26}$	$6.00^{+1.38}_{-0.80}$	$0.25^{+0.05}_{-0.05}$
AzV 22	14.2	Si II – Si III	1.80	67 ± 10	5.22	0.38	−7.14	−1.17	145	30	10.7 ± 2.9	0.31 ± 0.08	$21.94^{+2.18}_{-2.33}$	$21.65^{+2.06}_{-2.22}$	$7.18^{+0.87}_{-0.97}$	$0.18^{+0.02}_{-0.02}$
AzV 393	13.3	He I – Mg II	1.60	109 ± 16	5.53	0.48	−8.01	−1.09	151	30	17.8 ± 5.3	0.49 ± 0.13	$30.41^{+3.68}_{-4.02}$	$29.23^{+8.51}_{-10.12}$	$5.16^{+0.76}_{-0.60}$	$0.30^{+0.09}_{-0.11}$
AzV 343	12.0	He I – Mg II	1.98	49 ± 8	4.65	0.31	−6.14	−0.75	160	35	8.6 ± 2.4	0.13 ± 0.03	$13.21^{+1.12}_{-1.07}$	$12.90^{+1.32}_{-0.81}$	$13.30^{+1.99}_{-1.55}$	$0.08^{+0.01}_{-0.01}$
AzV 324	12.5	He I – Mg II	2.20	48 ± 8	4.70	0.06	−6.18	−0.83	156	25	13.5 ± 3.5	0.09 ± 0.03	$13.73^{+1.17}_{-1.07}$	$13.56^{+1.24}_{-1.04}$	$12.54^{+1.79}_{-1.46}$	$0.09^{+0.01}_{-0.01}$

In Table A.1, M_{init}, $M_{\rm evo}$, and ages of the stars are derived using an updated Bayesian inference method (Bronner et al. in prep) that is similar to BONNSAI (Schneider et al. 2014) applied to Brott et al. (2011) SMC evolutionary tracks. The average uncertainty in $T_{\rm eff}$ is $\Delta T_{\rm eff} = 1$ kK. In the uncertainties of centrifugal force-corrected surface gravity $\log g_c$, we take into account the fitting uncertainty of $\log g$ and the uncertainty of the projected rotational velocity $\upsilon_{\rm rot} \sin i$ and the radius R_*. We find a mean uncertainty of $\Delta \log g_c = 0.2$ dex. The uncertainty in radial velocity $\upsilon_{\rm rad}$ measurements is dominated by the velocity resolution of the UBV part of the spectrum which is $\Delta\upsilon \approx 45$ km s^{-1}. The total extinction A_V ($\Delta A_V \approx 0.02$ mag), absolute V-band magnitude $M_{\rm V}$, and bolometric correction $BC_{\rm V}$ are produced from the SED fits. $\Gamma_{\rm e}^{\rm spec}$ is subject to uncertainties of $\Delta\Gamma_{\rm e}^{\rm spec} \approx 0.2$ which takes into account the uncertainties of $M_{\rm spec}$ and $\log L_{\rm bol}$

Appendix B: Additional discussion on Z dependence

In parallel with the present study, Verhamme et al. (2025) have analysed a sample of ULLYSES/XShootU SMC B supergiants using KIWI-GA. They find broadly comparable mass-loss rates and wind momenta with respect to LMC B supergiants (Verhamme et al. 2024), in contrast with our results, despite having 13 stars in common with our sample.

This surprising result could be attributed to a number of issues. Firstly, the determination of robust wind parameters of late B supergiants in the SMC is particularly challenging due to the lack of wind diagnostics, and the current version of FASTWIND is known to have convergence difficulties below 14 kK (de Burgos et al. 2024b). These issues could have skewed KIWI-GA solutions to higher $D_{\rm mom}$. This is confirmed when examining the Hα fits of Verhamme et al. (2025), where the preferred solution overpredicts Hα emission. In addition, their derived $T_{\rm eff}$ often deviates quite significantly from the usual spectral type – temperature scale of B supergiants (see e.g. Lanz & Hubeny 2007; Trundle et al. 2007; Nieva 2013). By way of example, Verhamme et al. (2025) obtained a lower $T_{\rm eff}$ for AzV 410 (B0.7 Iab) than NGC330 ELS 4 (B2.5 Ib).

Appendix C: Additional discussion of wind parameters and the bi-stability jump

In Fig. C.1, we show the wind efficiency parameter $\eta = \frac{\dot{M}\upsilon_\infty}{L_{\rm bol}/c}$ versus $T_{\rm eff}$. We find that η smoothly decreases with $T_{\rm eff}$. One extreme outlier is the hypergiant AzV 393, which has a very high $\dot{M}$. Another outlier is AzV 456, which has a very low η. This is due to its υ_∞, which is lower by ≈300 km s^{-1} compared to AzV 327, which has a very similar $T_{\rm eff}$.

Appendix D: CNO diagnostics

Table D.1 shows the diagnostic lines used to constrain the surface abundances of carbon, nitrogen, and oxygen. It also shows the spectral type range in which each metal line is used.

Appendix E: $\upsilon_{\rm black}$ and $\upsilon_{\rm edge}$

In Table E.1 we present the measured $\upsilon_{\rm edge}$ and $\upsilon_{\rm black}$ from each line for all our sample.

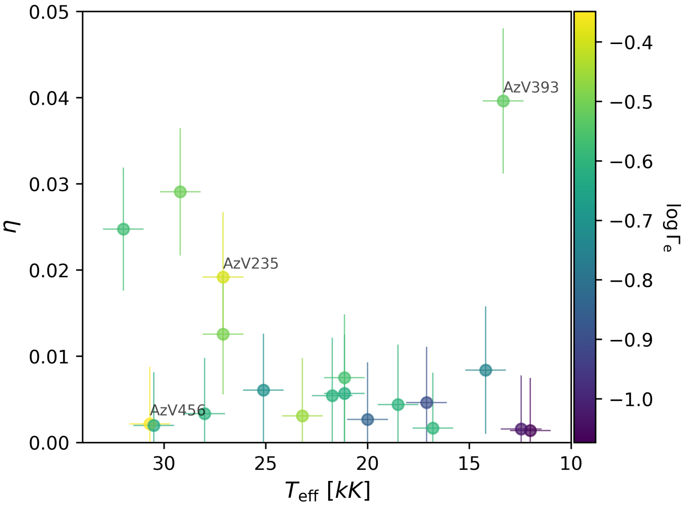

Fig. C.1: Wind efficiency $\eta = \frac{\dot{M}\upsilon_\infty}{L_{\rm bol}/c}$ in terms of $T_{\rm eff}$.

Table D.1: Line diagnostics for determination of CNO elemental abundances.

line	Sp. T.
C IV $\lambda\lambda$5801 − 5811	O9-B0
C III $\lambda\lambda$4647 − 4650	O9-B3
C III λ5696	O9-B3
C II λ4070	B0-B8
C II λ4267	B0-B8
C II $\lambda\lambda$6578 − 6582	B0-B8
N III λ4097	O9-B0.5
N III $\lambda\lambda$4379	O9-B0.5
N III $\lambda\lambda$4510 − 4515	O9-B0
N III $\lambda\lambda$4634 − 4641	O9-B0
N II λ3995	B1-B8
N II λ4447	B1-B8
N II $\lambda\lambda\lambda$4601 − 4607 − 4614	B1-B8
N II λ4630	B1-B8
O III $\lambda\lambda$3261 − 3265	O9-B1
O III λ3760	O9-B1
O III λ5592	O9-B1
O II λ4254	B0-B6
O II λ4367	B0-B6
O II $\lambda\lambda$4415 − 4417	B0-B6
O II $\lambda\lambda$4638 − 4641	B0-B6
O I $\lambda\lambda\lambda$7772–7774–7775	B7-B8

Table E.1: $v_{\rm edge}$ and $v_{\rm black}$ for the stars in our sample.

	$v_{\rm edge}$					
Target	Si IV 1393Å	Si IV 1403Å	C IV 1548Å	Al III 1855Å	Al III 1863Å	$\overline{v_{\rm black}}/\overline{v_{\rm edge}}$
AzV 469	2190	-	2133	-	-	0.84
AzV 372	1944	-	-	-	-	0.78
AzV 456	1655	-	2327	-	-	-
AzV 327	1935	-	1976	-	-	-
AzV 235	1653	-	1633	-	-	-
AzV 215	1935	-	2060	-	-	-
AzV 104	-	-	1255	-	-	-
AzV 410	1218	-	1280	-	-	-
AzV 242	1105	-	1270	-	-	-
AzV 96	972	-	956	-	-	-
AzV 264	827	-	-	-	-	-
AzV 175	222	-	224	-	-	-
Sk 191	620	594	600	582	-	0.76
AzV 18	507	-	472	-	-	-
ELS-04	515	-	-	-	-	-
AzV 187	589	588	575	-	-	-
AzV 22	190	173	206	222	230	-
AzV 393	319	-	279	-	-	-
AzV 343	285	251	282	-	-	-
AzV 324	259	207	220	210	-	-

	$v_{\rm black}$					
Target	Si IV 1393Å	Si IV 1403Å	C IV 1548Å	Al III 1855Å	Al III 1863Å	$\overline{v_{\rm black}}$ km s^{-1}
AzV 469	-	-	1814	-	-	1814 ± 100
AzV 372	-	-	1516	-	-	1516 ± 100
Sk 191	474	440	451	-	-	455 ± 45

Notes. We obtain $v_{\rm edge}$ and v_∞ from all the available P Cygni line profiles in the UV. Single velocity measurement from each line is subject to an uncertainty $\Delta v = 30$ km s^{-1} which takes into account the velocity resolution of the UV spectra and the uncertainty in the radial velocity correction, which were added in quadrature.

Appendix F: Comparison to literature

Table F.1 contains our derived values for $T_{\rm eff}$, $\log g$, $L_{\rm bol}$, $\log \dot{M}$, β, and $f_{\rm vol,\infty}$, along with literature values from Trundle et al. (2004), Trundle & Lennon (2005), Bernini-Peron et al. (2024), Backs et al. (2024), and Bestenlehner et al. (2025). The volume-filling factor for studies that used the optically thick clumping implementation in FASTWIND is calculated from the equation introduced in Sander et al. (2024) following:

$$f_{\rm vol,\infty} = \frac{(1-f_{\rm ic})^2}{f_{\rm cl} - 2f_{\rm ic} + f_{\rm ic}^2}, \tag{F.1}$$

where $f_{\rm cl} = \langle\rho^2\rangle/\langle\rho\rangle^2$ describes the contrast between the density in the clump and the mean density, and $f_{\rm ic}$ describes the contrast between the clump density and the density of the inter-clump medium.

In addition to literature values, Table F.1 in includes $\log \dot{M}$ values obtained from LIME (Sundqvist et al. 2025) . LIME is a user-friendly and fast online tool that allows for the estimation of the mass-loss rates of stars using an iterative semi-analytic approach using an extension of the Castor et al. (1975) concept. By including a detailed list of atomic lines, but avoiding a numerical solution for the equation of motion and the stellar atmosphere, the tool can estimate $\dot{M}$ on the fly, in contrast to the recipes discussed in Section 4.3, which result from approximating sets of detailed numerical models. The input parameters we used for LIME are our derived $T_{\rm eff}$, $L_{\rm bol}$, $M_{\rm spec}$, mass fractions of H, He, C, N, O, and the mean mass fractions for elements heavier than oxygen presented in Vink et al. (2023). In Fig. F.1 we compare our obtained values $T_{\rm eff}$, $\log g$, $L_{\rm bol}$, $\log \dot{M}$, and $\log \dot{M}_{\rm smooth} = \log \dot{M}/\sqrt{f_{\rm vol,\infty}}$ to the values in the literature. We find that our $T_{\rm eff}$ values are consistent with values from the literature within the uncertainties. The only exception is AzV 18 for which Bestenlehner et al. (2025) find a value of $T_{\rm eff} = 23.7$ kK compared to our value of 18.5 kK. Similarly, our $\log g$ is generally in agreement with values from the aforementioned studies. We find that $\log g$ values obtained by Bestenlehner et al. (2025) are systematically lower than ours.

We find a similar picture for $L_{\rm bol}$, where our derived values are consistent with the values presented in the literature. The exception in this case is some of the values obtained by Bestenlehner et al. (2025), mainly for AzV 235, AzV 242, and AzV 18, for which we obtain $\log L_{\rm bol}/L_\odot = 5.86, 5.71, 5.45$, respectively, compared to 6.01, 5.28, 5.75 from Bestenlehner et al. (2025).

The $\dot{M}$ comparison tells a different story. We find that for the most part, the values of $\dot{M}$ are inconsistent, and our $\dot{M}$ is generally lower. The mean difference between our $\log \dot{M}$ and those from Bestenlehner et al. (2025), Backs et al. (2024), Bernini-Peron et al. (2024), Trundle et al. (2004) and Trundle & Lennon (2005), and LIME are $\approx -0.4, -0.7, -0.5, -0.9, -0.3$ dex, respectively. The immediate contributors to this inconsistency are the choice of clumping implementation (optically-thin vs optically-thick clumping and clumping law), the derived values for clumping parameters, and the derived/adopted values of β and v_∞. Furthermore, the differences in $T_{\rm eff}$, $\log g$, and $\epsilon_{\rm He}$ propagate to the estimated $\dot{M}$. Another obvious issue is the usage of various codes that implement different methods for solving the radiative transfer equations. Therefore, when all these issues are taken into account, differences up to a factor of 3 in $\dot{M}$ can be expected.

We can test if the values of clumping parameters are a major cause of the inconsistency in the mass-loss rates by comparing the ‘smooth’ mass-loss rates, $\dot{M}_{\rm smooth}$. This shows a similar

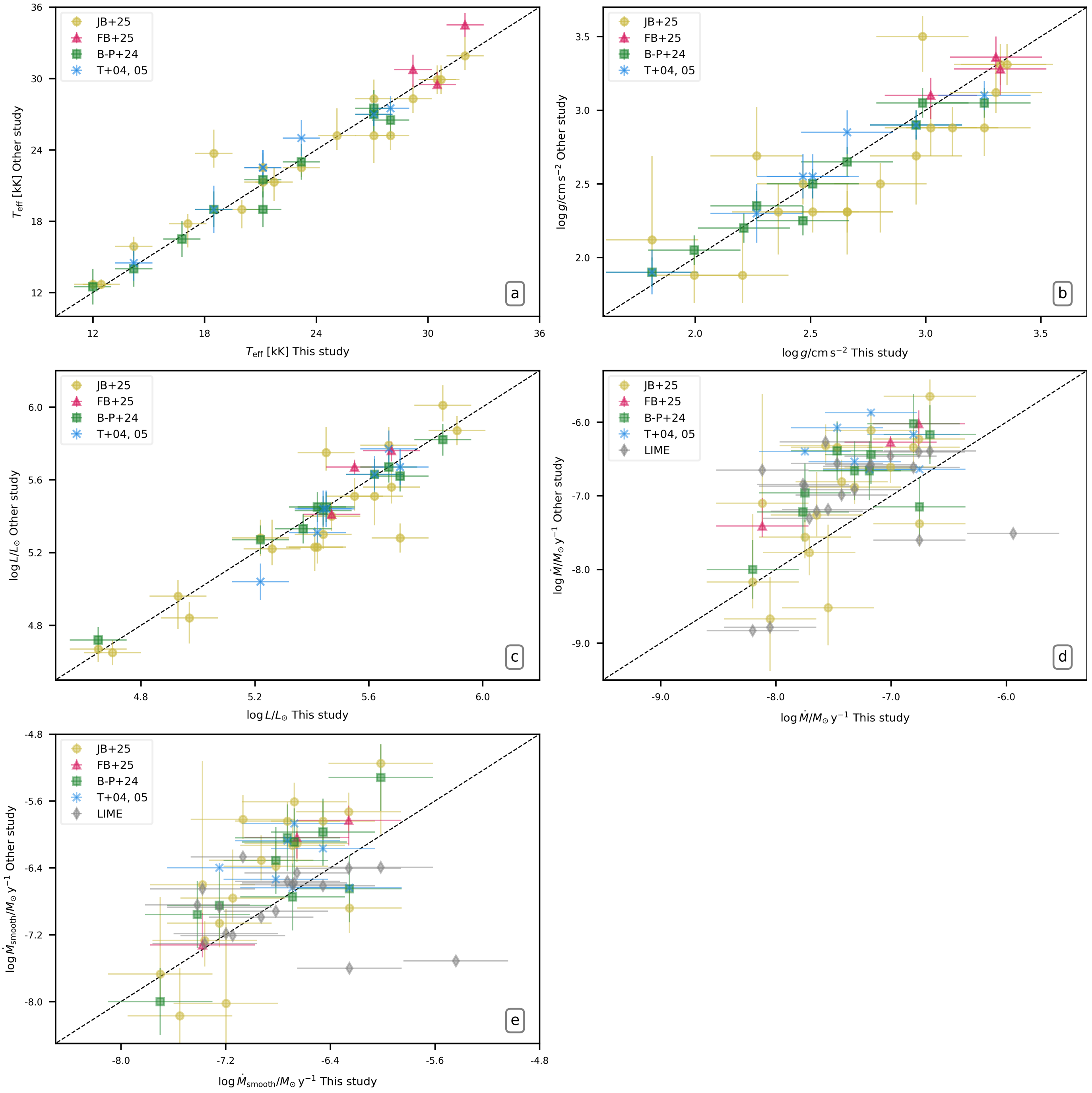

Fig. F.1: Comparison of our obtained parameters to literature values. a: $T_{\rm eff}$ comparison, b: $\log g$ comparison, c: $L_{\rm bol}$ comparison, d: $\log \dot{M}$ comparison, e: $\log \dot{M}_{\rm smooth}$ comparison. Pink triangles: comparison to Backs et al. (2024). Green squares: comparison to Bernini-Peron et al. (2024). Blue Xs: comparison to Trundle et al. (2004) and Trundle & Lennon (2005). Grey diamonds: comparison to values obtained from LIME Sundqvist et al. (2025).

trend; our $\dot{M}_{\rm smooth}$ is systematically lower than other studies, except for the values obtained from LIME, but now the mean difference between our $\dot{M}_{\rm smooth}$ and those from the literature are considerably lower and are $\approx -0.4, -0.4, -0.3, -0.4, 0.2$ dex, respectively. Therefore, the derived/adopted values of the clumping parameters can significantly affect the resulting mass loss rates and are a major factor in the discrepancy seen in $\dot{M}$.

Table F.1: Comparison of derived parameters to previous studies.

Target	$T_{\rm eff}$ kK	$\log g$ $\rm cm\,s^{-2}$	$\log L$ $L_\odot$	$\log \dot{M}$ $M_\odot\,\rm yr^{-1}$	$f_{\rm vol,\infty}$	β	Ref.	wavelength	Code
AzV 469	32.0	3.30	5.55	−7.00	0.2	1.0	This study	UV+OPT	C
	$31.9^{+1.2}_{-1.6}$	$3.12^{+0.1}_{-0.2}$	$5.51^{+0.1}_{-0.1}$	$-6.61^{+0.2}_{-0.2}$	0.1	1.0	JB+25	OPT	F
	$34.5^{+1.0}_{-1.0}$	$3.36^{+0.1}_{-0.1}$	$5.67^{+0.0}_{-0.0}$	$-6.27^{+0.2}_{-0.1}$	0.34	1.1	FB+24	UV+OPT	F
	-	-	-	−6.46	-	-	LIME	-	-
AzV 372	29.2	3.02	5.68	−6.76	0.1	1.0	This study	UV+OPT	C
	$28.3^{+1.2}_{-1.2}$	$2.88^{+0.2}_{-0.1}$	$5.56^{+0.1}_{-0.1}$	$-6.23^{+0.2}_{-0.2}$	0.1	1.0	JB+25	OPT	F
	$30.8^{+1.5}_{-1.2}$	$3.1^{+0.2}_{-0.1}$	$5.76^{+0.1}_{-0.0}$	$-6.02^{+0.3}_{-0.2}$	0.42	1.8	FB+24	UV+OPT	F
	-	-	-	−6.4	-	-	LIME	-	-
AzV 456	30.7	3.35	5.91	−7.57	0.1	1.0	This study	UV+OPT	C
	$29.9^{+1.2}_{-1.2}$	$3.31^{+0.1}_{-0.1}$	$5.87^{+0.1}_{-0.1}$	$-6.32^{+0.2}_{-0.3}$	0.1	1.0	JB+25	OPT	F
	-	-	-	−6.27	-	-	LIME	-	-
AzV 327	30.5	3.32	5.47	−8.12	0.03	1.0	This study	UV+OPT	C
	$29.9^{+1.2}_{-1.2}$	$3.31^{+0.1}_{-0.1}$	$5.40^{+0.1}_{-0.1}$	$-7.1^{+0.4}_{-1.5}$	0.1	1.0	JB+25	OPT	F
	$29.5^{+0.2}_{-1.0}$	$3.28^{+0.2}_{-0.1}$	$5.41^{+0.0}_{-0.0}$	$-7.41^{+0.2}_{-0.4}$	0.67	0.8	FB+24	UV+OPT	F
	-	-	-	−6.65	-	-	LIME	-	-
AzV 235	27.1	2.99	5.86	−6.66	0.05	1.5	This study	UV+OPT	C
	$28.3^{+1.2}_{-1.6}$	$3.5^{+0.2}_{-0.1}$	$6.01^{+0.1}_{-0.1}$	$-5.65^{+0.8}_{-0.2}$	0.1	1.0	JB+25	OPT	F
	27.5	3.05	5.82	−6.17	0.02	2.4	BP+24	UV+OPT	C
	-	-	-	−6.39	-	-	LIME	-	-
AzV 215	27.1	2.96	5.62	−7.17	0.1	1.7	This study	UV+OPT	C
	$25.2^{+2.3}_{-1.2}$	$2.69^{+0.3}_{-0.1}$	$5.51^{+0.2}_{-0.1}$	$-6.11^{+0.2}_{-0.2}$	0.1	1.0	JB+25	OPT	F
	27.0	2.9	5.63	−6.44	0.2	2.8	BP+24	UV+OPT	C
	$27.0^{+1.0}_{-1.0}$	$2.9^{+0.1}_{-0.1}$	5.63	−5.87	1	1.4	T+04	OPT	F
	-	-	-	−6.58	-	-	LIME	-	-
AzV 104	28.0	3.25	5.42	−7.75	0.1	1.0	This study	UV+OPT	C
	$25.2^{+1.2}_{-1.2}$	$2.88^{+0.2}_{-0.1}$	$5.23^{+0.1}_{-0.1}$	$-7.56^{+0.3}_{-0.2}$	0.1	1.0	JB+25	OPT	F
	26.5	3.05	5.45	−6.96	0.6	0.5	BP+24	UV+OPT	C
	$27.5^{1.0}_{-1.0}$	$3.1^{0.1}_{-0.1}$	5.31	−6.4	1	1.0	T+04	OPT	F
	-	-	-	−6.87	-	-	LIME	-	-
AzV 410	25.1	3.12	5.26	−7.65	0.1	1.0	This study	UV+OPT	C
	$25.2^{+1.2}_{-2.3}$	$2.88^{+0.2}_{-0.1}$	$5.22^{+0.1}_{-0.2}$	$-7.26^{+0.3}_{-0.6}$	0.1	1.0	JB+25	OPT	F
	-	-	-	−7.21	-	-	LIME	-	-
AzV 242	23.2	2.66	5.71	−7.47	0.03	3.1	This study	UV+OPT	C
	$22.5^{+0.8}_{-0.8}$	$2.31^{+0.1}_{-0.1}$	$5.28^{+0.1}_{-0.1}$	$-6.34^{+0.2}_{-0.2}$	0.1	1.0	JB+25	OPT	F
	23.0	2.65	5.62	−6.39	0.2	1.8	BP+24	UV+OPT	C
	$25.0^{+1.5}_{-1.5}$	$2.85^{+0.2}_{-0.2}$	5.67	−6.08	1	2.0	T+05	OPT	F
	-	-	-	−6.56	-	-	LIME	-	-
AzV 96	21.7	2.66	5.41	−7.43	0.1	2.6	This study	UV+OPT	C
	$21.3^{+1.6}_{-1.2}$	$2.31^{+0.3}_{-0.2}$	$5.23^{+0.1}_{-0.1}$	$-6.81^{+0.2}_{-0.3}$	0.1	1.0	JB+25	OPT	F
	-	-	-	−6.99	-	-	LIME	-	-
AzV 264	21.1	2.51	5.44	−7.32	0.1	3.0	This study	UV+OPT	C
	$21.3^{+0.8}_{-1.2}$	$2.31^{+0.1}_{-0.1}$	$5.3^{+0.1}_{-0.1}$	$-6.88^{+0.2}_{-0.3}$	0.1	1.0	JB+25	OPT	F
	21.5	2.5	5.43	−6.66	0.2	1.8	BP+24	UV+OPT	C
	$22.5^{+1.5}_{-1.5}$	$2.55^{+0.2}_{-0.2}$	5.44	−6.54	1	2.5	T+05	OPT	F
	-	-	-	−6.92	-	-	LIME	-	-
AzV 175	20.0	2.80	4.97	−7.55	0.2	1.0	This study	UV+OPT	C
	$19.0^{+1.6}_{-0.8}$	$2.5^{+0.3}_{-0.1}$	$4.84^{+0.1}_{-0.1}$	$-8.52^{+0.5}_{-1.1}$	0.1	1.0	JB+25	OPT	F
	-	-	-	−7.19	-	-	LIME	-	-

References. JB+25: (Bestenlehner et al. 2025). FB+24: (Backs et al. 2024), BP+24: Bernini-Peron et al. (2024), T+05: (Trundle & Lennon 2005), T+04: (Trundle et al. 2004)

Notes. Obtained using F: FASTWIND, C: CMFGEN. The mass-loss rates are not corrected for clumping.

Table F.1: Continued.

Target	T_{eff} kK	$\log g$ cm s^{-2}	$\log L$ $L_{\odot}$	$\log \dot{M}$ $M_{\odot}$ yr^{-1}	$f_{\mathrm{vol},\infty}$	β	Ref.	wavelength	Code
Sk 191	21.1	2.47	5.67	-6.81	0.2	2.5	This study	UV+OPT	C
	$22.5^{+0.8}_{-1.2}$	$2.5^{+0.1}_{-0.1}$	$5.79^{+0.1}_{-0.1}$	$-6.34^{+0.2}_{-0.2}$	0.1	1.0	JB+25	OPT	F
	19.0	2.25	5.67	-6.02	0.8	2.8	BP+24	UV+OPT	C
	$22.5^{1.5}_{-1.5}$	$2.55^{0.2}_{-0.2}$	5.77	-6.17	1	2.0	T+04	OPT	F
	-	-	-	-6.62	-	-	LIME	-	-
AzV 18	18.5	2.27	5.45	-7.19	0.1	3.5	This study	UV+OPT	C
	$23.7^{+1.2}_{-2.0}$	$2.69^{+0.1}_{-0.3}$	$5.75^{+0.1}_{-0.1}$	$-6.63^{+0.2}_{-0.2}$	0.1	1.0	JB+25	OPT	F
	19.0	2.35	5.45	-6.66	1.5	1.0	BP+24	UV+OPT	C
	$19.0^{+2.0}_{-2.0}$	$2.3^{+0.2}_{-0.2}$	5.44	-6.64	1	3.0	T+04	OPT	F
	-	-	-	-6.6	-	-	LIME	-	-
NGC330-ELS-04	17.1	2.36	4.93	-7.71	0.2	1.0	This study	UV+OPT	C
	$17.8^{+2.0}_{-0.8}$	$2.31^{+0.3}_{-0.2}$	$4.96^{+0.2}_{-0.1}$	$-7.77^{+0.3}_{-0.2}$	0.1	1.0	JB+25	OPT	F
	-	-	-	-7.31	-	-	LIME	-	-
AzV 187	16.8	2.21	5.37	-7.77	0.2	1.0	This study	UV+OPT	C
	16.5	2.2	5.33	-7.22	0.3	2.2	BP+24	UV+OPT	C
	-	-	-	-6.84	-	-	LIME	-	-
AzV 22	14.2	1.81	5.22	-6.75	0.1	2.5	This study	UV+OPT	C
	$15.9^{+0.8}_{-0.8}$	$2.12^{+0.1}_{-0.6}$	$5.28^{+0.1}_{-0.1}$	$-7.38^{+0.3}_{-0.2}$	0.1	1.0	JB+25	OPT	F
	14.0	1.9	5.27	-7.15	0.1	3.7	BP+24	UV+OPT	C
	$14.5^{+1.5}_{-1.5}$	$1.9^{+0.2}_{-0.2}$	5.04	-6.64	1	1.0	T+04	OPT	F
	-	-	-	-7.6	-	-	LIME	-	-
AzV 393	13.3	1.61	5.53	-5.94	0.1	2.5	This study	UV+OPT	C
	-	-	-	-7.51	-	-	LIME	-	-
AzV 343	12.0	2.00	4.65	-8.2	0.1	1.0	This study	UV+OPT	C
	$12.7^{+0.4}_{-0.4}$	$1.88^{+0.2}_{-0.1}$	$4.67^{+0.1}_{-0.1}$	$-8.17^{+0.4}_{-0.9}$	0.1	1	JB+25	OPT	F
	12.5	2.05	4.72	-8.0	1.0	2.0	BP+24	UV+OPT	C
	-	-	-	-8.83	-	-	LIME	-	-
AzV 324	12.5	2.21	4.70	-8.05	0.1	1.0	This Study	UV+OPT	C
	$12.7^{+0.4}_{-0.4}$	$1.88^{+0.2}_{-0.3}$	$4.65^{+0.1}_{-0.1}$	$-8.67^{+0.7}_{-0.6}$	0.1	1	JB+25	OPT	F
	-	-	-	-8.78	-	-	LIME	-	-

References. JB+25: (Bestenlehner et al. 2025). FB+24: (Backs et al. 2024), BP+24: Bernini-Peron et al. (2024), T+05: (Trundle & Lennon 2005), T+04: (Trundle et al. 2004)

Notes. Obtained using F: FASTWIND, C: CMFGEN. The mass-loss rates are not corrected for clumping.